Axial compression behaviors of steel shear-keyed tubular columns: Numerical and analytical studies

Kashan Khan[a], Zhihua Chen[a,b,c], Jiadi Liu[a], Konstantinos Daniel Tsavdaridis[d], Keerthan Poologanathan[e]

[a]*Department of Civil Engineering, Tianjin University, Tianjin, China*

[b]*State Key Laboratory of Hydraulic Engineering Simulation and Safety, Tianjin, China*

[c]*Key Laboratory of Coast Civil Structure and Safety, Tianjin University, Tianjin, China*

[d]*School of Science & Technology, Department of Engineering, City, University of London (UK)*

[e]*Department of Mechanical and Construction Engineering, Northumbria University (UK)*

Abstract: This study developed a finite element model (FEM) and reported parametric and analytical studies on the axial compression behaviors of shear-keyed tubular columns in modular steel structures (MSS). The accuracy of the developed FEM was validated using 36 tests in references. The parametric study designed 108 FEMs to investigate initial imperfection, shear-key height (L_t), thickness (t_t), steel tube length (D), width (B), thickness (t_c), and height (L_c) influence. The typical load-shortening response showed elastic, inelastic, and recession stages, with failure modes of inward and outward sinusoidal pairs of local buckling. Increasing t_t, L_t, t_c, D, or B improved strength and stiffness, while L_c or slenderness (L_c/r) adversely affected the stiffness and ductility linearly. Besides, it ensured by validations that prediction equations in conventional design standards overestimated the compressive resistance, requiring modifications.

Keywords: Axial compression behaviors; Steel shear-keyed tubes; Finite element modeling; Experimental validations; Prediction equations

1 Introduction

Modular steel structure (MSS) comprises an onsite assembly of ready-made room-sized volumetric modules [1]. It has shown time efficiency [2], cost-effectiveness [3], high quality [4], improved safety [5], and reduced environmental impacts [6]. Column discontinuity distinguishes it from traditional steel structures (TSS) [7]. Corner-supported load-bearing steel modules resist loads via corner columns, providing space flexibility and a clear load transfer path [8–10]. Thus, they can extend to multi-story structures, as depicted in **Fig. 1(a)** [3,11]. They achieve outstanding strength, ductility, robustness, rigidity, durability, and lightness via steel-hollow section (SHS) columns to withstand loads [12–14]. The structural behavior and integrity of MSS mainly rely on the modules and their deformation coordination [15], ensured by a reliable inter-modular connection (IMC) [16]. Hence, welded [17], bolted [16], and pre-stressed [18,19] IMC are used at modules' corners to achieve structural integrity. However, technical difficulties, such as the robustness, instability, and complexity of interior connection tying, require effective measures because weak IMCs can affect the MSS's safety [20,21]. Thus, numerous joints between SHS columns have been proposed to address these concerns. Studies have been summarized in recently published review articles on IMC [1,16,22–27].

The shear-keyed IMC provides robust and efficient module connectivity at corners. Chen et al. [28,29], Khan et al. [30–32], and Peng et al. [33–36] applied non-welded hollow-shaped shear-keyed IMC in multi-story corner-supported MSS, demonstrating its applicability in real projects, as shown in **Fig. 1(a,b)**. Several welded, non-welded, or bolted shear-keyed IMC, including the solid or hollow box, threaded, cruciform, or socket-shaped join columns to ensure appropriate module connectivity and eliminate discreteness, are listed in Ref. [26]. Besides, different shear-keyed tubes and IMC have been studied, including experimental research by Hajimohammadi et al. [37]. They observed that raising the loading angle from 0^0 to 45^0 reduces shear keys' ultimate resistance, turning ASME-B1.1, BS-3580, and ISO/TR-16224 unsuitable. Chen et al. [28,29] discovered that shear-keyed IMC causes column tearing due to the shear and bending stresses. Bowron [38], Khan et al. [30–32], and Pang et al. [39] found non-welded and fully-bolted shear keys as semi-rigid while offering horizontal connectivity to columns. However, columns at shear-key zones generated significant stresses. The grouted shear-keyed tube was discovered by Dai et al. [40,41] to resist a load rigidly. Ma et al. [42], Deng et al. [43], and Zhang et al. [44] observed that shear resistance was offered by welded and bolted shear keys, but the absence of interior module fixity resulted in their rotations around columns. Nadeem et al. [45] presented an IMC with a self-locking shear key. They witnessed good resistance to slip and lateral forces [37]. However, geometrical imperfections causing installation issues were disregarded, impacting tube buckling behavior [9]. Welded [46] or bolted [47] shear-keyed tubes' lateral performance revealed adequate uplift resistance, ductility, and continuity to columns. Still, column tearing and beam-column connection failure was noticeable.

Recently, research focused on post- and pre-stressed shear-keyed IMC. For instance, Liew et al. [48,49] and Chen et al. [18] noted that shear-keyed IMC effectively provides lateral load resistance. Sanches et al. [50,51] determined that shear-key thickness governs the shear-keyed tube lateral force resistance through friction. Sandblasting or expanding the contact area increases the shear-slip resistance of shear-keyed tubes, as per Lacey et al. [52,53]. Although investigations mainly focused on lateral behavior, it can be seen that most shear-keyed IMC used shear keys inside tubes without welding or bolting. They observed that lateral and shear resistance was affected by the shear-key thickness and cross-section; however, shear-keyed tube axial compression behavior is unclear. Typically, buckling resistances and joint rotation are ignored, assuming shear keys and columns are tightly welded, leading to a conservative design. Because they have been studied and used in MSS projects, compression investigations on non-welded shear-keyed tubes are necessary.

Modules integrated with SHS using shear keys exhibit superior structural performance compared to cold-formed C-sections [1,2]. Traditional standards yielded conservative outcomes on the compression behavior of cold-formed columns [54]; however, Khan et al. [12–14] verified non-conservative findings for hot-rolled MSS tubular walls. Significant research has been performed on the tubes' compressive behavior. Still, their assumptions and conclusions were exclusive to TSS standard tubes with continuity at both or one end. Conversely, MSS's integrated modules cause tube discontinuities. Moreover, the studies above provide little information on shear-keyed tubes, which results in different boundary conditions, effective lengths, critical load, and ultimate resistance [55]. Unless unique details are not accounted for, conventional standards compatibility for shear-keyed columns becomes questionable. Additionally, tube designs disregarding shear-keyed IMC are unsuitable because they do not account for varying flexural rigidities of tubes at the mid-height and ends. Hence, this study investigated the shear-keyed columns' axial compression behaviors by developing a finite element model (FEM) and validating its accuracy with the 36 tests on standard and shear-keyed tubes. The influence of initial imperfection, shear-key height and thickness, and steel tube length, width, thickness, and height was investigated. Finally, traditional design standards' predictions applicability was examined to evaluate the ultimate resistances of shear-keyed tubes.

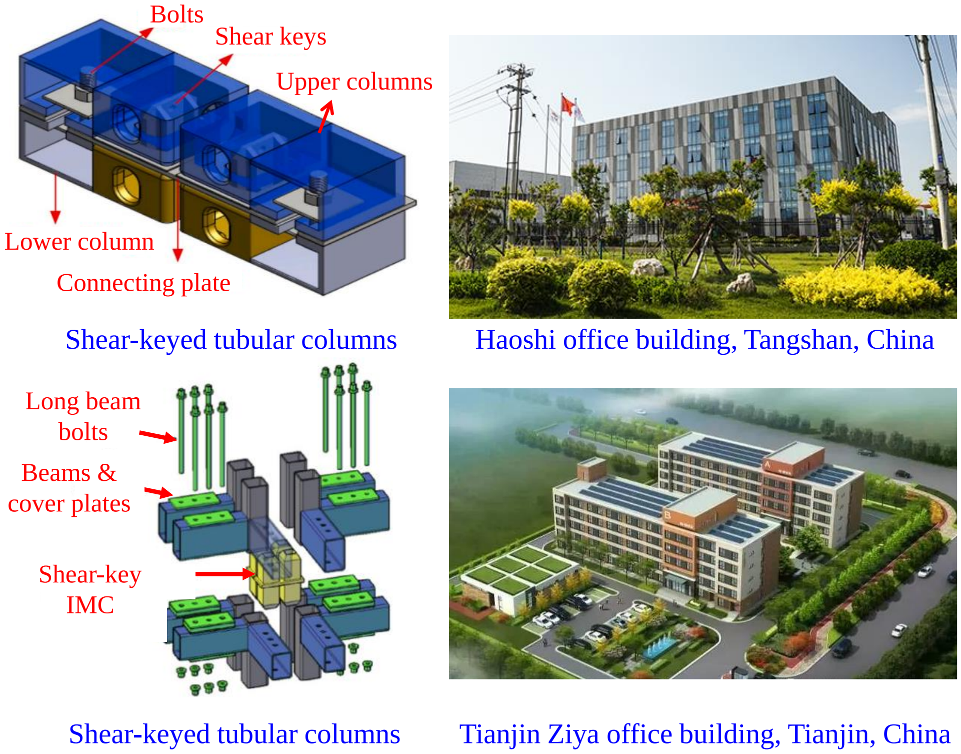

(a) Corner-supported modules with shear-keyed IMC (**Designed by the research team**) [28,29]

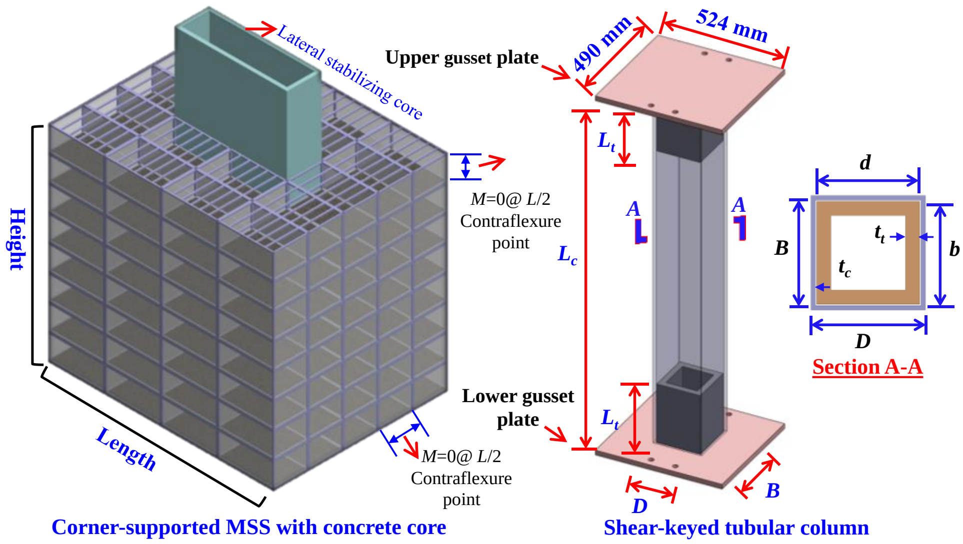

(b) Typical MSS with shear-keyed tubular columns details under consideration

Fig. 1 Applications of corner-supported MSS with shear-keyed tubes

2 Literature on experimental studies on SHS tubes

2.1 Combined axial and lateral loading

Chen et al. [28,29] evaluated shear-keyed IMC structural behavior with axial and lateral loadings on 12 shear-keyed frames. The axial and lateral loads were applied to the top free column via the column loading technique, with the lower column, ceiling, and floor beams functioning as rotational hinges. **Table 1** shows specimen details.

2.2 Axial compression loading

Theofanous and Gardner [56,57] conducted compression tests on stubs and flexural tests on long tubes. Stubs were fixed, while long tubes were pin-ended. Hou et al. [58] and Khan et al. [12,13] compressed planar and C-shaped walls having five tubes in planar, whereas additional three tubes in the C-shaped sidewalls. A ceiling beam, angle support, and a floor beam were welded to tubes. Welded blocks were installed on the bolted ceiling and the floor beam to create pin-ended boundaries. All specimen details are depicted in **Table 2**.

Table 1 Specifications and results of combined axial and lateral loading on tubular columns

Sp. #	SHS Column (mm)	SHS Floor (mm)	SHS Ceiling (mm)	Stiff plate (mm)	Axial load (kN)	Tube (#)	f_y (MPa)	f_u (MPa)	E_s (GPa)	$P_{u,Test}$ (kN)	$P_{u,FE}$ (kN)	$\frac{P_{u,Test}}{P_{u,FE}}$	Refs.
S1	150×150×8	150×250×8	150×150×8	No	286	1	425	575	200	114	120	0.95	[28,29]
S2	150×150×8	150×250×8	150×150×8	10	286	1	425	575	200	186	165	1.12	
QS1	150×150×8	150×250×8	150×150×8	No	286	1	425	575	200	83	81	1.02	
										-104	-120	0.86	
QS2	150×150×8	150×150×8	150×150×8	10	286	1	425	575	200	120	132	0.91	
										-139	-125	1.11	
QS3	150×150×8	150×250×8	150×150×8	10	286	1	425	575	200	163	124	1.31	
										-186	-165	1.12	
QS4	150×150×8	150×250×8	150×150×8	10	143	1	425	575	200	144	131	1.09	
										-171	-167	1.02	
SC1	150×150×8	150×250×8	150×150×8	No	286	2	425	575	200	251	265	0.94	
SC2	150×150×8	150×250×8	150×150×8	10	286	2	425	575	200	398	393	1.01	
QSC1	150×150×8	150×250×8	150×150×8	No	286	2	425	575	200	206	264	0.78	
										-235	-272	0.86	
QSC2	150×150×8	150×150×8	150×150×8	10	286	2	425	575	200	259	265	0.97	
										-309	-259	1.19	
QSC3	150×150×8	150×250×8	150×150×8	10	286	2	425	575	200	331	396	0.83	
										-366	-385	0.95	
QSC4	150×150×8	150×250×8	150×150×8	10	143	2	425	575	200	379	383	0.98	
										-407	-395	1.03	
Mean												**1.00**	
Cov												**0.13**	

f_y, f_u, E_s, $P_{u,\,Test}$, and $P_{u,\,FE}$ define yield strength, ultimate strength, elastic modulus, and ultimate resistance via tests and FE

Table 2 Details and outcomes of axial compression loading on tubular columns

Sp. #	D/a_c (mm)	B/b_c (mm)	t_c (mm)	L_c (mm)	Tube (#)	SHS (types)	$f_{y,w}$ (MPa)	$f_{u,w}$ (MPa)	$E_{s,w}$ (GPa)	$f_{y,C}$ (MPa)	$f_{u,C}$ (MPa)	$E_{s,C}$ (GPa)	$P_{u,Test}$ (kN)	$P_{u,FE}$ (kN)	$\frac{P_{u,Test}}{P_{u,FE}}$	Refs.
AS1	60	60	3	240	1	Square	755	839	209	885	1026	212	615	631	0.97	[57]
AS2	80	80	4	332	1	Square	679	773	199	731	959	210	919	920	1.00	
AS3	80	40	4	238	1	Rectangle	734	817	199	831	962	213	710	704	1.01	
AS4	100	100	4	400	1	Square	586	761	198	811	917	206	1030	1059	0.97	
AS5	60	60	3	2000	1	Square	755	839	209	885	1026	212	162	179	0.91	
AS6	60	60	3	1600	1	Square	755	839	209	885	1026	212	232	224	1.03	
AS7	60	60	3	1200	1	Square	755	839	209	885	1026	212	327	362	0.90	
AS8	60	60	3	800	1	Square	755	839	209	885	1026	212	447	471	0.95	
AS9	80	80	4	1200	1	Square	679	773	199	731	959	210	672	673	1.00	
AS10	80	80	4	2000	1	Square	679	773	199	731	959	210	362	381	0.95	
AS11	80	40	4	1600	1	Rectangle	734	817	199	831	962	213	160	167	0.96	
AS12	80	40	4	1200	1	Rectangle	734	817	199	831	962	213	237	247	0.96	

AS13	80	40	4	800	1	Rectangle	734	817	199	831	962	213	367	360	1.02	
AS14	121	76	2	242	1	Elliptical	193	380	676				234	225	1.04	[56]
AS15	121	76	3	242	1	Elliptical	194	420	578				444	443	1.00	
AS16	80	80	3	2815	5	Square	441	521	206				1287	1254	1.03	[12–14,58]
AS17	80	80	5	2815	5	Square	403	480	206				1829	1735	1.05	
AS18	100	80	3	2815	5	Rectangle	425	506	206				1495	1407	1.06	
AS19	140	80	4	2815	5	Rectangle	391	522	206				2222	2101	1.06	
AS20	140	80	6	2815	5	Rectangle	359	509	206				2812	2704	1.04	
AS21	160	80	5	2815	5	Rectangle	403	480	206				3027	2767	1.09	
AS22	200	80	10	2815	5	Rectangle	365	500	206				4805	5105	0.94	
AS23	100	80	3	2815	11	Rectangle	425	506	206				3208	3154	1.02	
AS24	160	80	5	2815	11	Rectangle	403	480	206				6373	6028	1.06	
Mean															**1.00**	
Cov															**0.05**	

$E_{s,w}$, $f_{y,w}$, $f_{u,w}$, $E_{s,c}$, $f_{y,c}$, $f_{u,c}$, D, B, L_c, and t_c define the tubes' flat wall and corner regions' elastic modulus, yield strength, ultimate strength, tube's length, width, height, and thickness; a_c and b_c, elliptical tube's longest and shortest diameter

Table 3 Details of compressive resistances of shear-keyed tubes using code prediction equations

Sp. #	D (mm)	B (mm)	t_c (mm)	L_c (m)	EC3 Class	$P_{u,EC3}$ (kN)	CSA Class	$P_{u,CSA}$ (kN)	AISC Class	$P_{u,AISC}$ (kN)	GB Class	$P_{u,GB}$ (kN)	f_y (MPa)	P_u (kN)
FS-46	200	200	5	3.0	C4	724	C4	645	S	1014	B	1283	380	837
FS-58	200	200	5	1.0	C4	766	C4	676	S	1102	B	1454	380	852
FS-47	200	200	7	3.0	C2	1885	C2	1640	NS	1650	B	1773	380	1523
FS-59	200	200	7	1.0	C2	2065	C2	1836	NS	1825	B	2013	380	1516
FS-60	200	200	8	1.0	C1	2348	C2	2087	NS	2074	B	2289	380	1796
FS-26	200	200	8	1.2	C1	2330	C2	2078	NS	2063	B	2269	380	1781
FS-25	200	200	8	1.5	C1	2303	C2	2060	NS	2041	B	2231	380	2040
FS-27	200	200	8	1.8	C1	2275	C2	2034	NS	2016	B	2192	380	1780
FS-28	200	200	8	2.4	C1	2213	C2	1961	NS	1953	B	2108	380	1778
FS-29	200	200	8	3.0	C1	2141	C2	1862	NS	1874	B	2014	380	1782
FS-30	200	200	8	3.6	C1	2053	C2	1741	NS	1782	B	1905	380	1782
FS-61	200	200	9	1.0	C1	2627	C2	2335	NS	2322	B	2561	380	1948
FS-49	200	200	9	3.0	C1	2394	C2	2080	NS	2095	B	2251	380	1971
FS-70	150	150	10	1.5	C1	2050	C1	1829	NS	1815	C	1876	380	1761
FS-71	180	180	10	1.5	C1	2529	C1	2262	NS	2243	C	2442	380	1807
FS-72	200	200	10	1.5	C1	2847	C1	2546	NS	2524	C	2705	380	1829
FS-73	220	220	10	1.5	C1	3164	C2	2827	NS	2805	B	3037	380	1841
FS-74	250	250	10	1.5	C1	3641	C3	3247	NS	3224	B	3544	380	1903
FS-85	160	80	8	1.5	C1	1310	C1	1006	NS	1032	C	1103	380	1220
FS-86	200	120	8	1.5	C1	1751	C2	1551	NS	1544	B	1667	380	1498
FS-87	220	140	8	1.5	C2	2014	C3	1796	NS	1783	B	1932	380	1635
FS-88	250	180	8	1.5	C3	2472	C3	2211	NS	2192	B	2390	380	1855

$P_{u,EC3}$, $P_{u,CSA}$, $P_{u,AISC}$, $P_{u,GB}$, P_u, and Cov define ultimate compressive resistance via EC3:1-1, CSA S16, AISC360-16, GB50017, FEA, and coefficient of variation

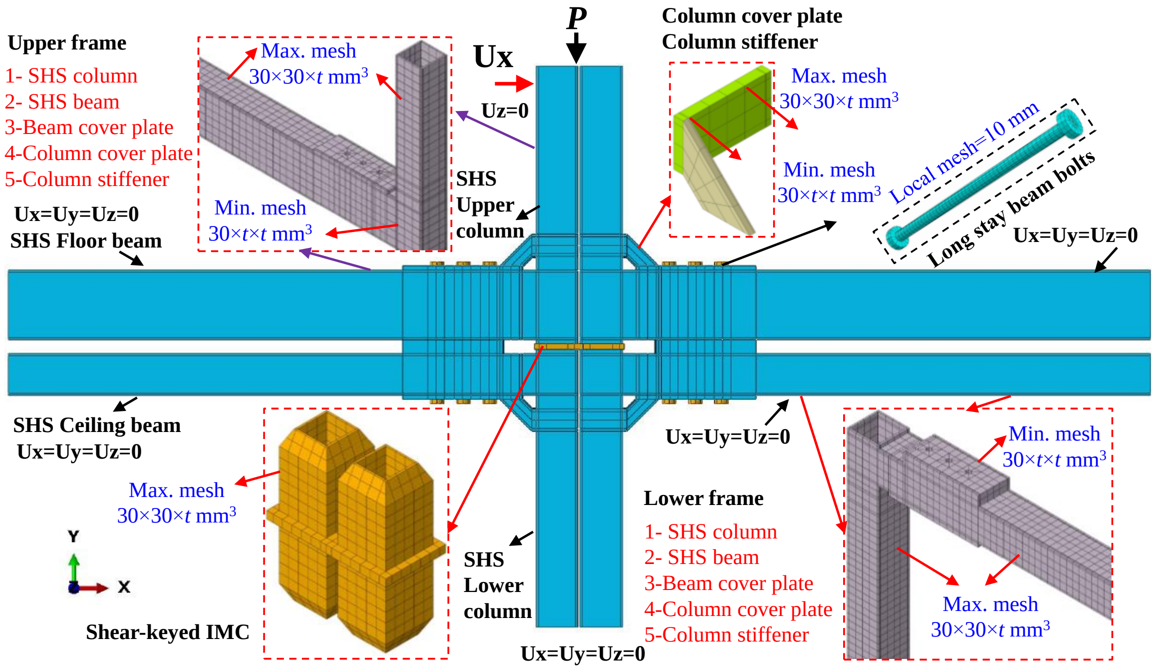

Fig. 2 FEM details of a shear-keyed frame by Chen et al. [28,29]

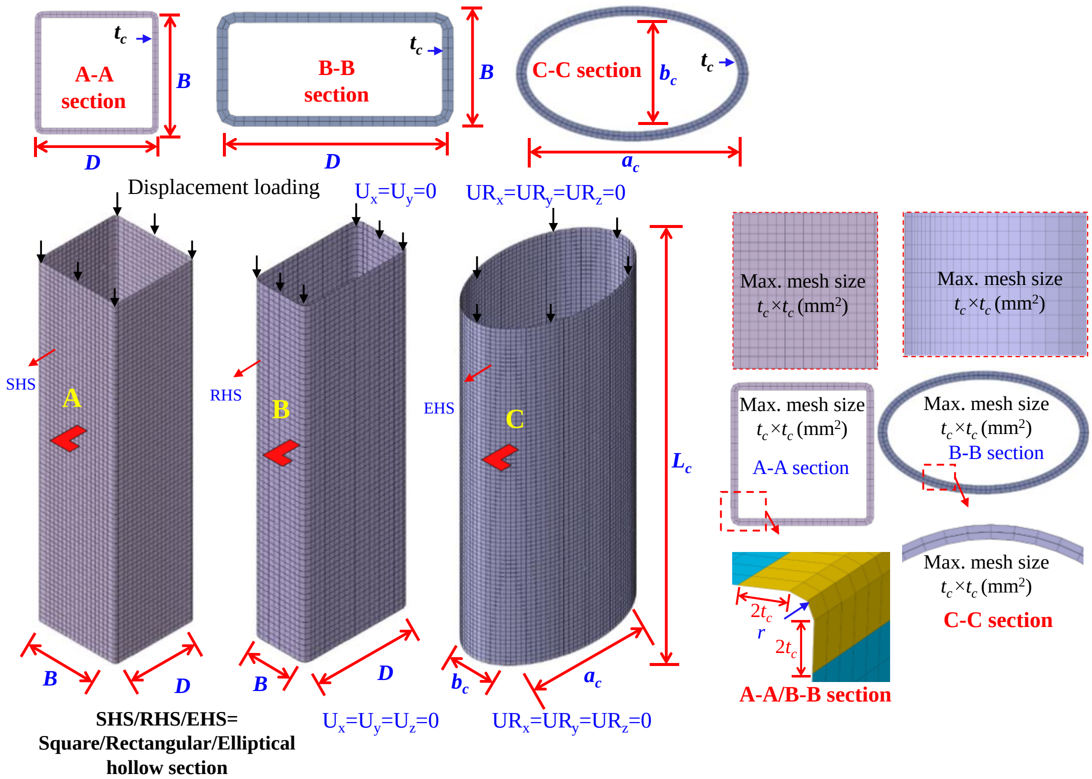

Fig. 3 FEM details of tubes by Theofanous and Gardner [57]

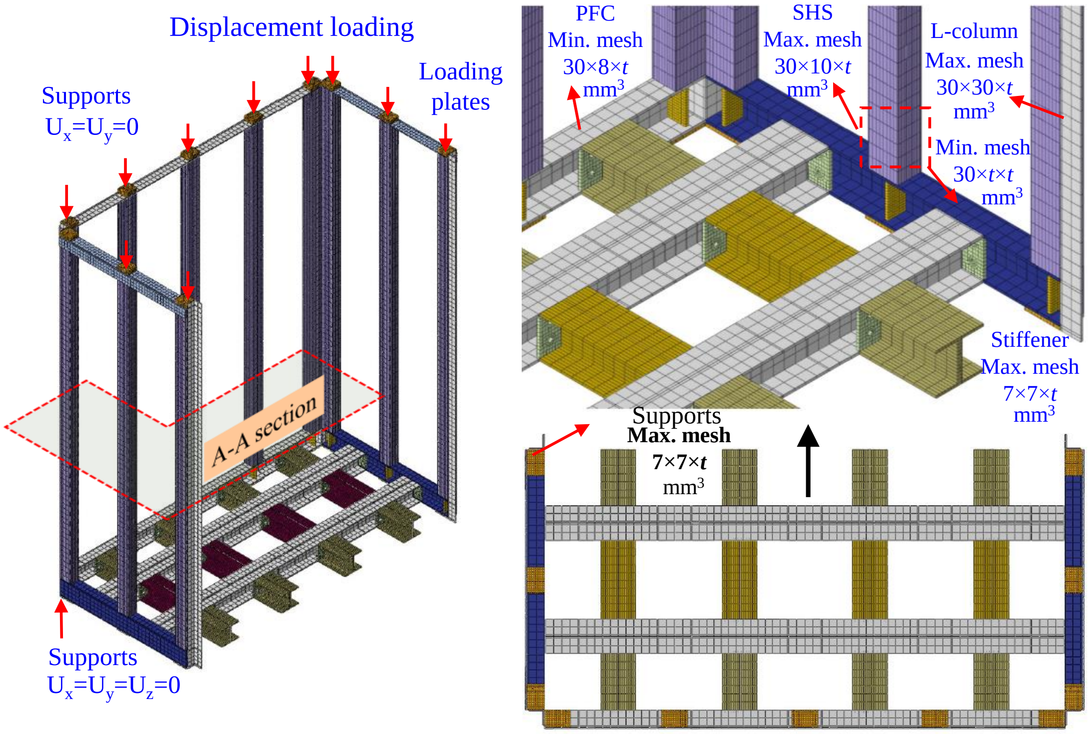

3D view **A-A section**

Fig. 4 FEM details of tubular walls by Hou et al. [58] and Khan et al. [12,13]

3 Nonlinear finite element modeling

The cited tests' findings in section 2 are used to build a reliable FEM of the shear-keyed tube to analyze the parametric effect.

3.1 Generalized finite element model

The modeling and finite element analysis (FEA) were performed using ABAQUS [59]. ABAQUS/Static general solver was used for tha validation of tests carried out on shear-keyed frames by Chen et al. [28,29]. Moreover, tests conducted by Theofanous and Gardner [56,57], Hou et al. [58], and Khan et al. [12,13] were validated using buckling and post-buckling analyses. Elastic buckling was performed with ABAQUS/Linear perturbation buckle-type solver using the subspace iteration method to determine the buckling loads and modes. Then ABAQUS/static Riks-type solver, a variant of the classical arc-length method, was adopted to determine the load-shortening and failure mechanism in the nonlinear analysis.

As depicted in **Fig. 2** and **Table 1**, the cover plates, stiffeners, beams, and columns were treated as single-frame components in the FEM of the shear-keyed frame. Bolt heads, shafts, and nuts were modeled without threads and without considering the bolt-to-hole gap. The FEM of cold-formed stainless-steel tubes is shown in **Fig. 3,** and that of hot-rolled tubular column walls is depicted in **Fig. 4**. Their structural members preserve **Table 2** dimensions. These FEMs modeled varying shape tubes, cover plates, stiffeners, beam bolts, angle columns, floor channels, angle ceiling beams, connecting plates with holes, and the floor chassis. This improves simulation accuracy, ensuring simulation on shear-keyed tubes' ultimate strength.

3.2 Constraints, loadings, interactions, and geometric imperfections

Following shear-keyed frames in [28,29], the lower columns' movement was restricted in all directions. The upper columns' were free with lateral displacement and axial loading applied in the vertical direction. There were constraints on beams in the vertical direction. Moreover, beams' and columns' out-of-plane movement and rotation were constrained, allowing them to rotate in-plane. Loading and boundary conditions on columns and beams were attained by defining the reference nodes on the cross-sections' midpoint with surface-based coupling constraints that limit the translation and rotation at the coupling nodes. Using the "penalty friction formulation," the contact between beams and bolts, neighboring columns and beams, and the column and the shear key was simulated as surface-to-surface contact (standard), with "hard contact" as the normal behavior and "finite sliding" as the tangential behavior. The friction coefficient used for penalty friction formulation was 0.3.

Following the experimental setup in [56,57], all degrees of freedom were restrained at the stub column cross-section ends, except for vertical translation for top-end nodes, to simulate displacement loading and allow vertical shortening. Similar constraints were applied to the flexural buckling FEMs of long tubes, except for the unrestrained rotational degree of freedom about the buckling axis, allowing pin-ended boundaries.

Surface-based coupling constraints were achieved to apply loads or boundary conditions to tube ends using kinematic coupling. The motion of a collection of (slave) nodes on end surfaces was coupled to the rigid body motion defined by the reference node on cross-sectional centers. Kinematic couplings were introduced by constraining the rotational and translational degrees of freedom at the coupling nodes. The membrane residual stresses due to seam-welding have a negligible effect on the ultimate capacity of stainless SHS. The residual stresses caused by the bending residual stresses are inherent in the material stress-strain properties. Consequently, residual stresses are not explicitly introduced into the FEMs [43,57,60,61]. Simulating geometric imperfections involved examining buckling shapes and comparing load-shortening curves from Refs. [56,57]. Initially, the eigenmode analysis obtained several buckling modes, followed by the nonlinear Riks analysis and selecting the closest buckling mode with test failure mode for applying geometric imperfections. Local geometric imperfections were applied to stubs, whereas local and global imperfections as eccentricity were applied to long columns. It was discovered that the failure mode of most test specimens, i.e., stubs or long tubes, was limited to the lowest buckling mode, i.e., the first buckling mode, consistent with test sources in Refs. [56,57]. According to Ref. [57], the study chose the local imperfection of $t_c/100$ and the global imperfection magnitude of $L_c/1500$.

Moreover, the motion of the top and bottom beams was restrained in hot-rolled tubular walls in all directions as Refs. [58] and [12,13]. In contrast, the bottom portion vertical movement and rotations were released to allow specimen shortening. In order to apply displacement loading and boundary conditions, surface-based kinematic coupling constraints were achieved by defining the reference nodes on cushion block centers above and below the ceiling and floor beams and restricting the rotational and translational degrees of freedom at the coupling nodes. Beams have been welded to cushion blocks, columns, and angles. Moreover, modular floors included welded floors and stringer beams; thus, the "tie constraint" with surface-to-surface contact was used, preventing their relative movement. Wall failure was not restricted to strength failure; it was caused by global instability beginning with the global buckling of the middle column of the front walls and the outer columns of the exterior sidewall columns as determined by Hou et al. [58] and Khan et al. [12,13]. Moreover, while using advanced analysis, member and frame imperfections are suggested to be modeled with a minimum value of $L_c/500$ and a maximum of $L_c/1000$, which are considerably larger and incorporate members' local geometric imperfections [62]. Therefore, buckling analysis considered the global instability mode and neglected local imperfections, as reported in Refs. [63,64] and [10]. The load and ultimate end-shortening appear to be better anticipated using the magnitude of $L_c/600$, which was incorporated into the FEM. This value of imperfection was obtained by comparing the load-shortening findings to those of test load-shortening curves.

3.3 Elements type and mesh sizes

The shear-keyed frame utilized hexagonally structured mesh controls with an eight-node linear brick, reduced integration, and Hourglass Control Element Type (C3D8R). Corners, edges, bolts, and holes have finely meshed with minimal mesh density, as shown in **Fig. 2**. Still, other regions utilized the maximum mesh sizes. It was discovered that $30\times30\times t$, $30\times t\times t$, and 10 mm were feasible mesh sizes for the upper and lower frame skeletons, shear-keyed IMC, cover plates, stiffeners, and beam bolts. Four-noded double-curved shell elements (S4R) were employed to discretize cold-formed thin-walled stainless steel tube sections, as shown in **Fig. 3.** All models used element sizes equal to the material thickness for corners and flat surfaces. Regarding corners, they have partitioned at a distance of $2t_c$ times from the edges of curved regions' root radii (*r*), assuming their geometry approximates circular arcs. The *r* values of tubes are computed from the source study Refs. [56,57]. Connecting plates with holes in walls used advanced hexagonal sweep mesh controls, whereas remaining deformable solid parts adopted the structured C3D8R element type. The feasible mesh sizes for SHS tubes, angle columns, stiffeners, connecting plates, PFC floor beams, and cushion blocks were determined to be $30 \times 10 \times t$, $30 \times 30 \times t$, $30 \times 8 \times t$, and $7 \times 7 \times t$, following Refs. [58] and [12,13], as displayed in **Fig. 4**. Stress singularity can be caused by mesh convergence, point loads, boundary conditions applied to point supports, sharp corners, small radius on corners, contact on sharp corners, fixed boundary conditions, and effect of local disturbances [65–72]. However, it does not affect displacement, deformation, and stress elsewhere as St. Venant's principle; thus, it was ignored [65–67,70,71].

3.4 Material simulation

The hot-rolled shear-keyed frames and multi-column walls neglect tube corner strengthening and root radii, as shown in **Figs. 2 and 4**. Moreover, the cold-forming method produces increased strength in the corner regions; thus, the enhanced strength was applied to corners that extended $2t_c$ beyond the curved corner regions into the flat portions of the stainless steel cross-section, as depicted in **Fig. 3** [56,57]. The corner material properties were applied to the corner and the neighboring flat regions up to $2t_c$. In contrast, flat wall properties were assigned to the remaining areas of the cross-section as per the techniques followed in Refs. [56,57] and [73–75]. The material properties essential for material definition in the FEM development and validation are listed in **Tables 1 and 2**. **Table 2** lists the material properties of the flat regions and the corner region from the corner to the flat sections by a distance of $2t_c$. As per C.6 of EN 1993-

1-5:2006 (E) [76], engineering stress-strain values can be converted into true ones using Eqns. (1) and (2). The chosen Poisson ratio is 0.3.

$$\sigma_T = \sigma_E(1 + \varepsilon_E) \quad (1)$$
$$\varepsilon_T = \ln(1 + \varepsilon_E) \quad (2)$$

where σ_E/ε_E are Engineering stress/strain while σ_T/ε_T True stress/strain.

3.5 Validations

Figure 5(a-ac) and Tables 1 and 2 compare FE and experimental load-shortening curves and test-to-prediction ratios, indicating FEMs predict shortening behavior accurately with minor differences in stiffness or post-ultimate recession. These deviations were induced by soft support, material models, modeling simplifications, and insufficient geometric imperfection simulations. According to the test-to-FE prediction ratios in **Table 1**, the FE's average estimations for 12 tests were 1.0 with a Cov of 0.13. Similarly, **Table 2** shows that the FE's average assessments for 24 tests were 1.0 with a Cov of 0.05, indicating minor prediction errors for P_u. **Figure 6** compares FEA-deformed shapes to experimental results, showing FEM can accurately anticipate failure behavior. For instance, columns gap widening, columns and beams fracture, local inward and outward buckling (IB and OB), global buckling (GB), stiffener bending, channel beam extrusion, angle weld fracture, and restraint effect. This ensures that the developed FEM could predict columns' axial compression behaviors at both the member and structural levels.

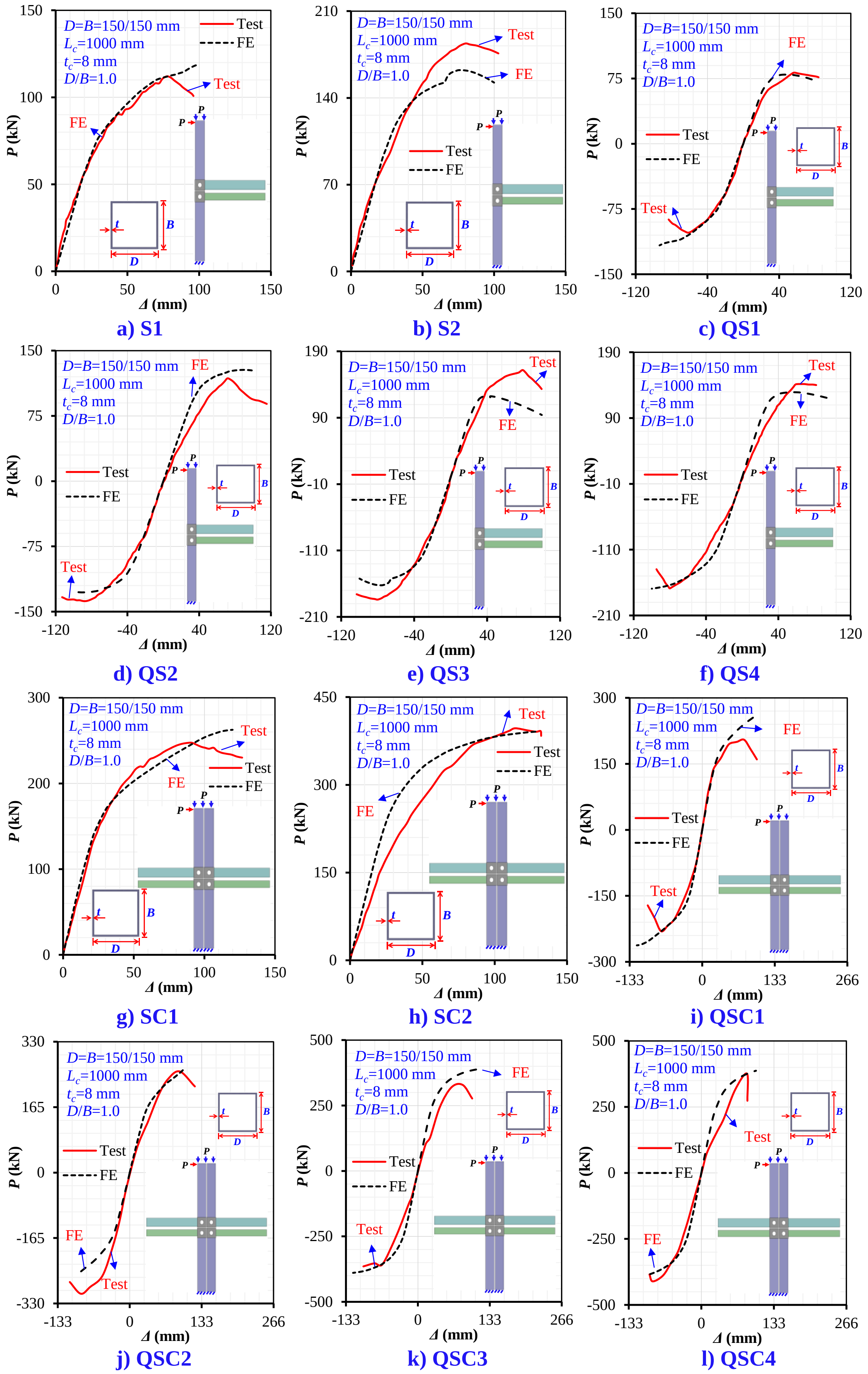
D=B=150/150 mm
L_c=1000 mm
t_c=8 mm
D/B=1.0
Test
FE
P (kN)
Δ (mm)
a) S1
b) S2
c) QS1
d) QS2
e) QS3
f) QS4
g) SC1
h) SC2
i) QSC1
j) QSC2
k) QSC3
l) QSC4

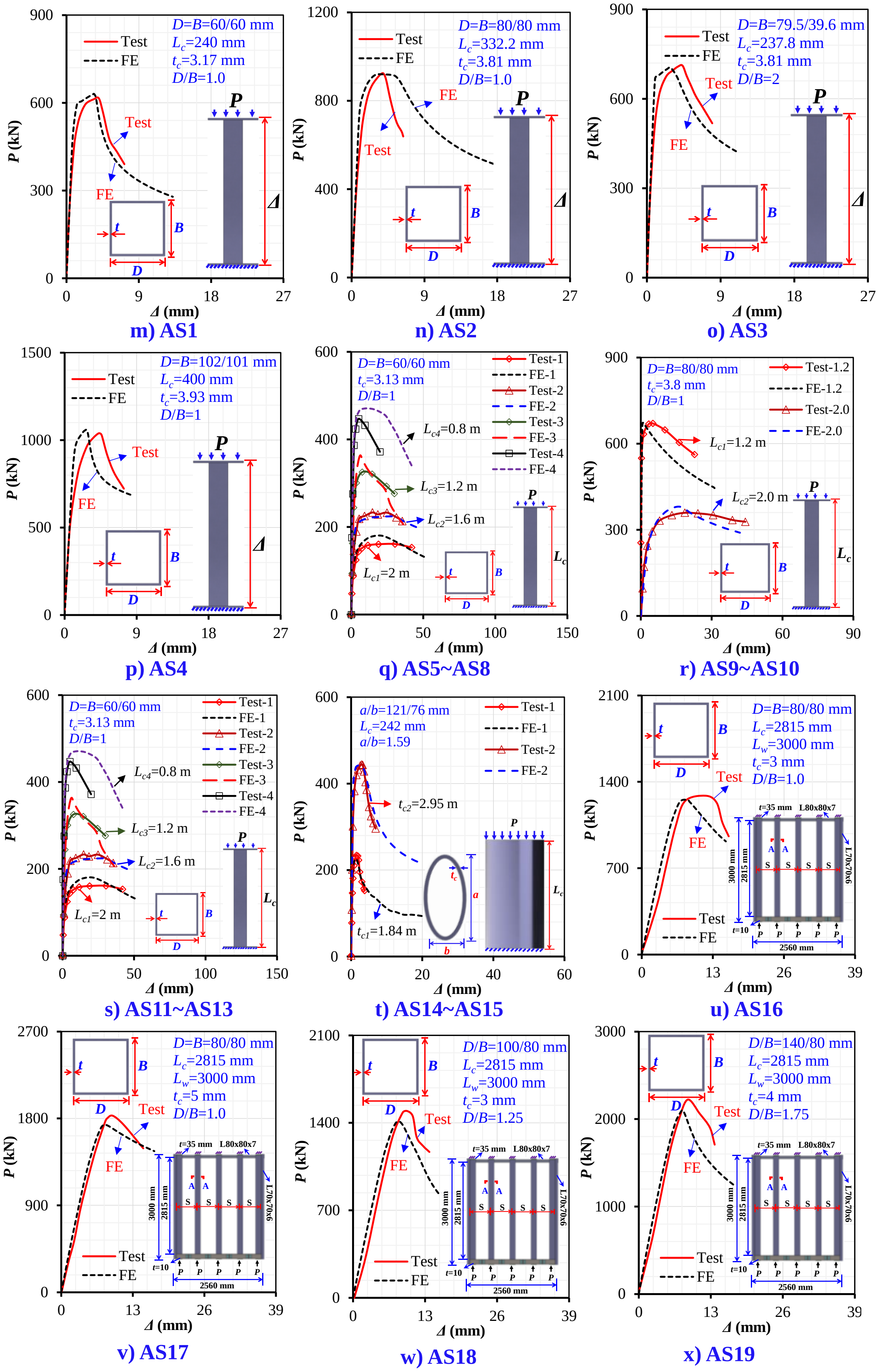
m) AS1
D=B=60/60 mm
L_c=240 mm
t_c=3.17 mm
D/B=1.0
n) AS2
D=B=80/80 mm
L_c=332.2 mm
t_c=3.81 mm
D/B=1.0
o) AS3
D=B=79.5/39.6 mm
L_c=237.8 mm
t_c=3.81 mm
D/B=2
p) AS4
D=B=102/101 mm
L_c=400 mm
t_c=3.93 mm
D/B=1
q) AS5~AS8
D=B=60/60 mm
t_c=3.13 mm
D/B=1
L_c4=0.8 m
L_c3=1.2 m
L_c2=1.6 m
L_c1=2 m
r) AS9~AS10
D=B=80/80 mm
t_c=3.8 mm
D/B=1
L_c1=1.2 m
L_c2=2.0 m
s) AS11~AS13
D=B=60/60 mm
t_c=3.13 mm
D/B=1
t) AS14~AS15
a/b=121/76 mm
L_c=242 mm
a/b=1.59
t_c2=2.95 m
t_c1=1.84 m
u) AS16
D=B=80/80 mm
L_c=2815 mm
L_w=3000 mm
t_c=3 mm
D/B=1.0
v) AS17
D=B=80/80 mm
L_c=2815 mm
L_w=3000 mm
t_c=5 mm
D/B=1.0
w) AS18
D/B=100/80 mm
L_c=2815 mm
L_w=3000 mm
t_c=3 mm
D/B=1.25
x) AS19
D/B=140/80 mm
L_c=2815 mm
L_w=3000 mm
t_c=4 mm
D/B=1.75
Test
FE
P (kN)
Δ (mm)

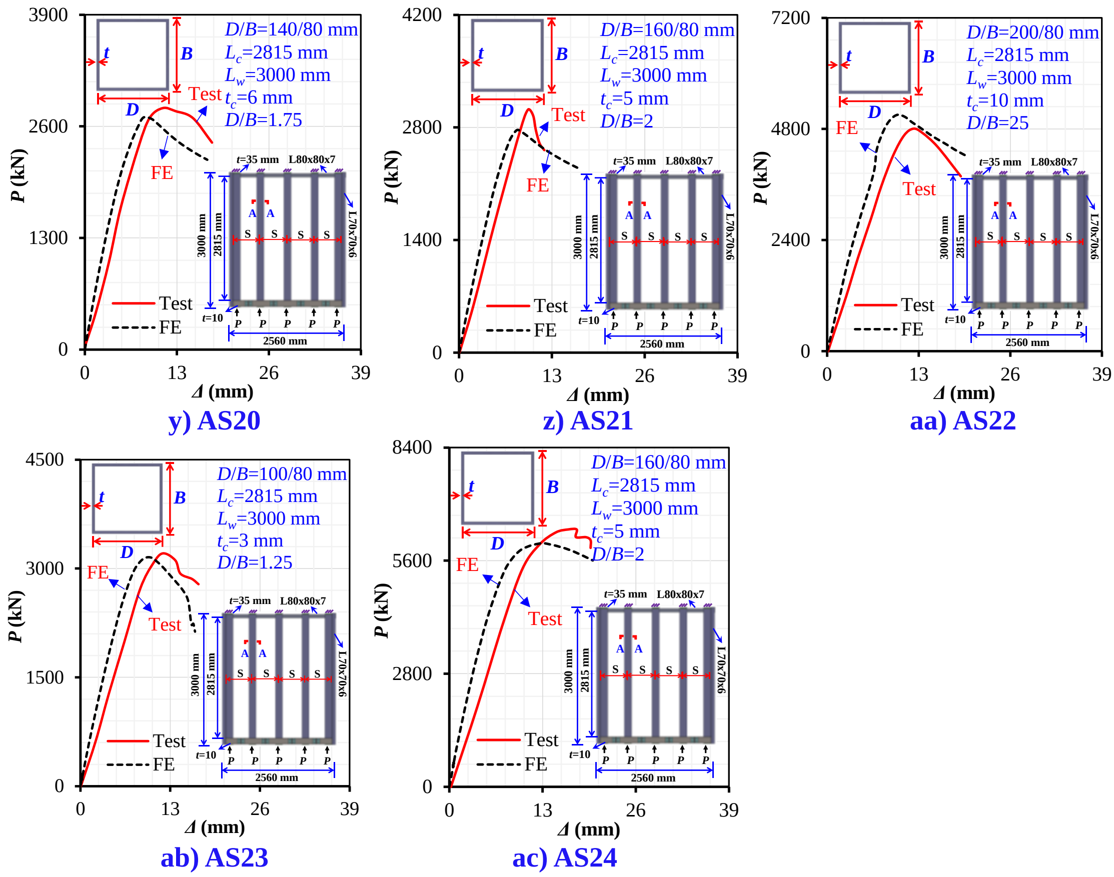

Fig. 5 Test to FE-predictions comparison

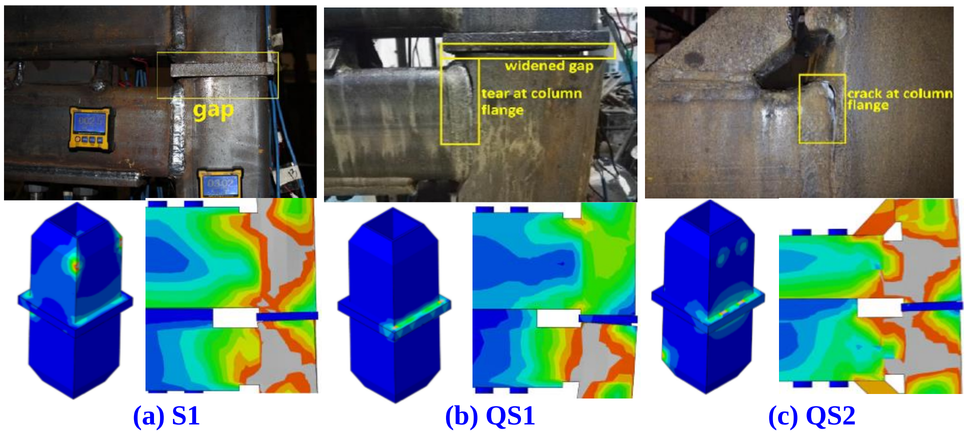

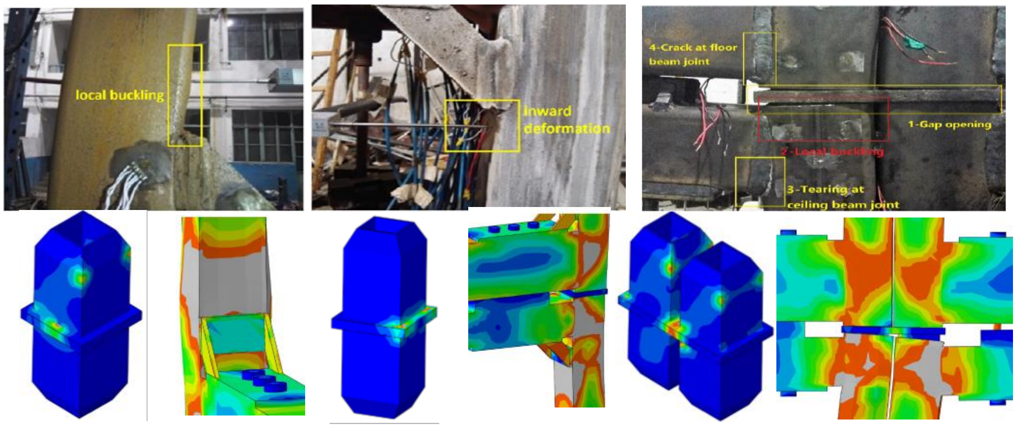

(d) QS3 (e) QS4 (f) SC1

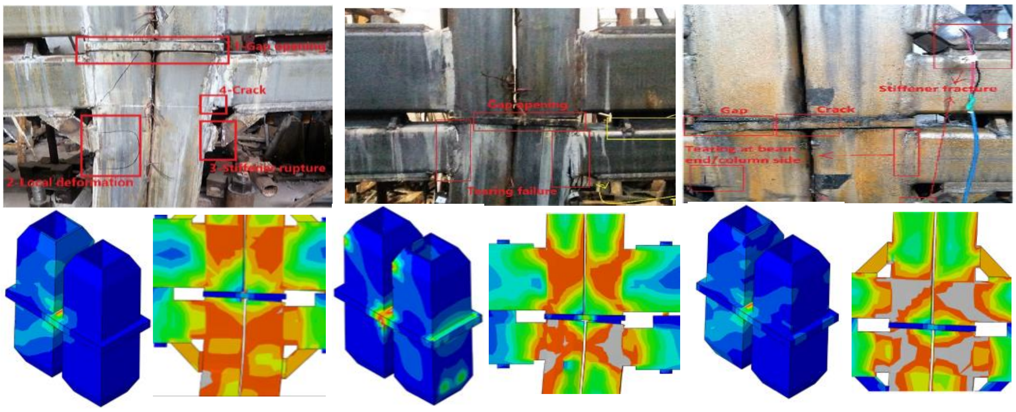

(g) SC2 (h) QSC1 (i) QSC2

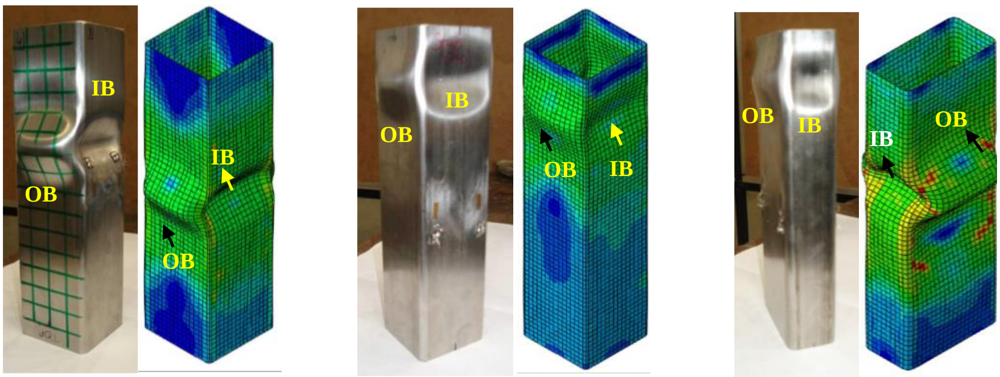

(j) 60×60×3 (k) 80×80×4 (l) 80×40×4

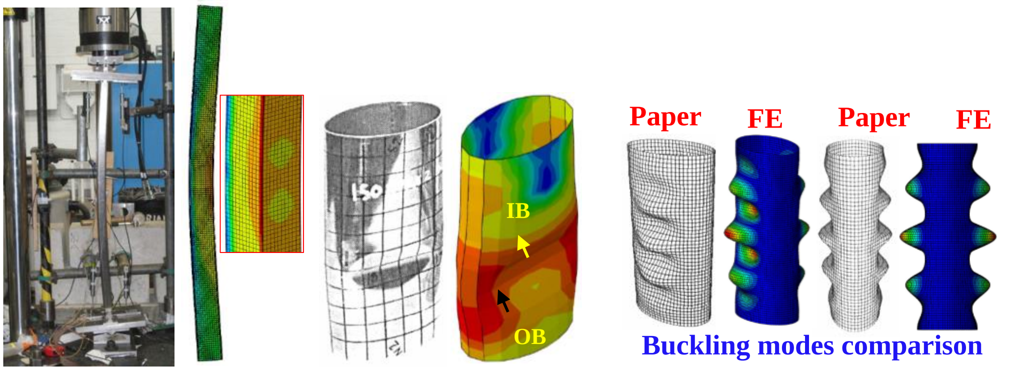

(m) 80×40×4-1600 (n) 121×76×2 (o) Elliptical SHS buckling mode

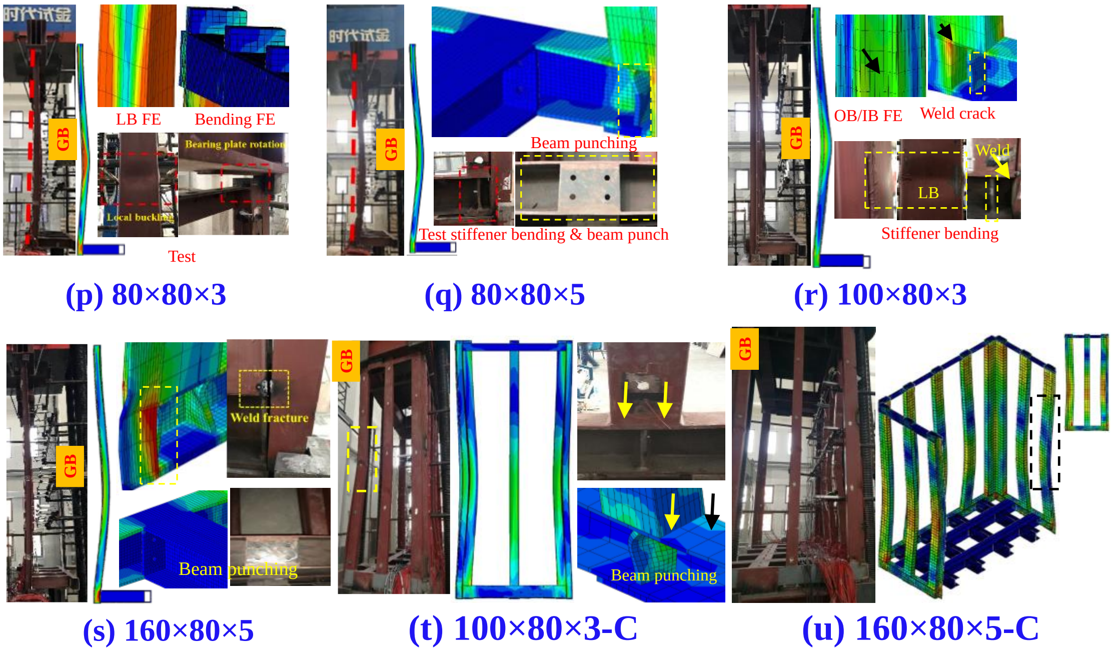

Fig. 6 Test to FE-failures comparison

4 Numerical studies on shear-keyed tubes in MSS

4.1 Investigated parameters and behavior details

A parametric study employing 108 validated FEMs investigated the effects of initial imperfection, shear-key height (L_t), thickness (t_t), steel tube height (L_c), width (B), length (D), and thickness (t_c) on the compressive behavior of shear-keyed tubes. These FEMs are categorized by varying t_t (15, 20, and 25 mm for given L_t of 100, 150, and 250 mm), L_t (75, 150, 250, and 300 mm with 15, 20, 25, and 35 mm t_t), L_c (1.2, 1.8, 2.4, 3.0 and 3.6 m for given L_t of 75, 150, 250, and 300 mm), t_c (5, 7, 8, and 9 mm with 1 and 3 m L_c, and for given L_t of 100, 150, and 250 mm), D/B (150/150, 180/180, 200/200, 220/220, 250/250, 160/80, 200/120, 220/140, and 250/180 mm for given L_t of 100, 150, and 250 mm), and imperfections (t_c/100, t_c/10, t_c/5, t_c/2, t_c, L_c/2000, L_c/1500, L_c/1000, L_c/500, D/20, D/8, and D/4). **Table 4** lists further information about these studies.

The behavior compares the ultimate compressive resistance (P_u), axial shortening (Δ_u), initial stiffness (K_e), and ductility index (DI) of shear-keyed tubes. The load-shortening curves of shear-keyed tubes can be used to determine the P_u and Δ_u. Moreover, it is possible to calculate the K_e using Eqn. 3. Similarly, DI can be calculated by Eqn. 4. Preand post-ultimate ductility of the shear-keyed tubes are represented by Δ_u and DI. **Table 4** lists each FEM's P_u, Δ_u, K_e, and DI values [77].

$$K_e = {}^{P_{45\%}}/_{\Delta_{45\%}} \tag{3}$$

$$DI = {}^{\Delta_{85\%}}/_{\Delta_u} \tag{4}$$

where $P_{45\%}$, $\Delta_{45\%}$ and $\Delta_{85\%}$ represent $0.45P_u$ and shortening at $P_{45\%}$ and $P_{85\%}$. **Figure 8(b)** shows the computation procedure for these terminologies [78].

Table 4 Detailed parametric results of shear-keyed tubes

Item	D (mm)	B (mm)	t_c (mm)	t_t (mm)	d (mm)	b (mm)	L_c (mm)	L_t (mm)	P_u (kN)	K_e (kN/mm)	Δ_u (mm)	DI Ratio
No Key	200	200	8	-	-	-	1500	-	2398	704	7.9	2.5
FS-1	200	200	8	15	180	180	1500	100	1346	471	16.4	2.9
FS-2	200	200	8	20	180	180	1500	100	1490	538	14.9	3.4
FS-3	200	200	8	25	180	180	1500	100	2031	623	10.8	2.5
FS-4	200	200	8	15	180	180	1500	150	1397	496	13.7	2.2
FS-5	200	200	8	20	180	180	1500	150	1518	570	14.9	2.0
FS-6	200	200	8	25	180	180	1500	150	1807	733	7.8	3.5
FS-7	200	200	8	15	180	180	1500	250	1657	572	9.9	3.3
FS-8	200	200	8	20	180	180	1500	250	1786	610	9.1	2.8
FS-9	200	200	8	25	180	180	1500	250	2099	659	9.8	2.4
FS-10	200	200	8	15	180	180	1500	75	1397	495	12.9	2.4
FS-11	200	200	8	15	180	180	1500	150	1397	496	13.7	2.2
FS-12	200	200	8	15	180	180	1500	250	1396	501	11.5	2.6
FS-13	200	200	8	15	180	180	1500	300	1397	501	13.0	2.3
FS-14	200	200	8	20	180	180	1500	75	1518	562	14.4	2.1
FS-15	200	200	8	20	180	180	1500	150	1518	570	14.9	2.0
FS-16	200	200	8	20	180	180	1500	250	1521	578	11.9	2.2
FS-17	200	200	8	20	180	180	1500	300	1523	590	9.6	2.5
FS-18	200	200	8	25	180	180	1500	75	1781	719	8.0	2.0
FS-19	200	200	8	25	180	180	1500	150	1807	733	7.8	3.5
FS-20	200	200	8	25	180	180	1500	250	1872	735	6.2	2.1
FS-21	200	200	8	25	180	180	1500	300	1875	736	6.7	2.1
FS-22	200	200	8	35	180	180	1500	75	1986	768	4.0	1.6
FS-23	200	200	8	35	180	180	1500	150	2030	790	4.2	2.9
FS-24	200	200	8	35	180	180	1500	250	2040	764	5.3	2.2
FS-25	200	200	8	35	180	180	1500	300	2040	787	6.7	1.6
FS-26	200	200	8	25	180	180	1200	75	1781	873	7.8	3.2
FS-27	200	200	8	25	180	180	1800	75	1780	618	7.3	2.2
FS-28	200	200	8	25	180	180	2400	75	1778	495	6.1	2.4
FS-29	200	200	8	25	180	180	3000	75	1782	404	7.1	2.2
FS-30	200	200	8	25	180	180	3600	75	1782	339	8.2	2.0
FS-31	200	200	8	25	180	180	1200	150	1806	883	8.0	2.2
FS-32	200	200	8	25	180	180	1800	150	1807	635	7.2	2.2
FS-33	200	200	8	25	180	180	2400	150	1806	487	7.2	2.3
FS-34	200	200	8	25	180	180	3000	150	1809	398	8.3	2.0
FS-35	200	200	8	25	180	180	3600	150	1807	340	7.8	2.2
FS-36	200	200	8	25	180	180	1200	250	1858	891	6.4	2.2
FS-37	200	200	8	25	180	180	1800	250	1875	628	6.9	1.9
FS-38	200	200	8	25	180	180	2400	250	1873	490	6.6	1.9
FS-39	200	200	8	25	180	180	3000	250	1876	405	6.7	1.9
FS-40	200	200	8	25	180	180	3600	250	1875	339	8.0	1.7
FS-41	200	200	8	25	180	180	1200	300	1859	891	5.7	2.7
FS-42	200	200	8	25	180	180	1800	300	1879	643	5.6	2.3
FS-43	200	200	8	25	180	180	2400	300	1877	498	5.7	2.4
FS-44	200	200	8	25	180	180	3000	300	1880	401	7.3	2.0
FS-45	200	200	8	25	180	180	3600	300	1880	340	7.7	2.0
FS-46	200	200	5	25	180	180	3000	100	837	136	14.3	1.4

FS-47	200	200	7	25	180	180	3000	100	1523	336	7.8	1.6
FS-48	200	200	8	25	180	180	3000	100	1800	399	8.5	1.8
FS-49	200	200	9	25	180	180	3000	100	1971	418	15.0	1.7
FS-50	200	200	5	25	180	180	3000	150	838	137	13.9	2.1
FS-51	200	200	7	25	180	180	3000	150	1537	329	8.0	1.4
FS-52	200	200	8	25	180	180	3000	150	1809	398	8.3	2.0
FS-53	200	200	9	25	180	180	3000	150	1971	422	12.9	1.8
FS-54	200	200	5	25	180	180	3000	250	837	137	13.4	1.5
FS-55	200	200	7	25	180	180	3000	250	1606	342	8.4	1.5
FS-56	200	200	8	25	180	180	3000	250	1876	405	6.7	1.9
FS-57	200	200	9	25	180	180	3000	250	1998	425	13.5	1.8
FS-58	200	200	5	25	180	180	1000	100	852	445	4.6	2.5
FS-59	200	200	7	25	180	180	1000	100	1516	755	7.5	2.2
FS-60	200	200	8	25	180	180	1000	100	1796	1017	8.4	3.0
FS-61	200	200	9	25	180	180	1000	100	1948	1098	8.3	2.7
FS-62	200	200	5	25	180	180	1000	150	850	445	4.9	2.4
FS-63	200	200	7	25	180	180	1000	150	1524	755	7.2	1.5
FS-64	200	200	8	25	180	180	1000	150	1798	1018	7.7	3.7
FS-65	200	200	9	25	180	180	1000	150	1950	1103	10.0	2.2
FS-66	200	200	5	25	180	180	1000	250	851	445	4.8	2.4
FS-67	200	200	7	25	180	180	1000	250	1561	753	7.0	1.7
FS-68	200	200	8	25	180	180	1000	250	1834	1029	5.3	2.8
FS-69	200	200	9	25	180	180	1000	250	1965	1150	5.8	3.1
FS-70	150	150	10	25	130	130	1500	100	1761	540	13.3	3.0
FS-71	180	180	10	25	160	160	1500	100	1807	688	14.9	3.2
FS-72	200	200	10	25	180	180	1500	100	1829	817	8.9	4.3
FS-73	220	220	10	25	200	200	1500	100	1841	823	9.9	4.2
FS-74	250	250	10	25	230	230	1500	100	1903	961	6.9	5.3
FS-75	150	150	10	25	130	130	1500	150	1762	637	16.2	3.0
FS-76	180	180	10	25	160	160	1500	150	1807	691	15.4	3.4
FS-77	200	200	10	25	180	180	1500	150	1828	821	9.3	5.0
FS-78	220	220	10	25	200	200	1500	150	1841	843	9.7	5.0
FS-79	250	250	10	25	230	230	1500	150	1903	967	7.1	7.2
FS-80	150	150	10	25	130	130	1500	250	1769	653	14.2	4.5
FS-81	180	180	10	25	160	160	1500	250	1811	719	13.4	4.0
FS-82	200	200	10	25	180	180	1500	250	1836	851	8.1	4.6
FS-83	220	220	10	25	200	200	1500	250	1849	1006	9.9	5.6
FS-84	250	250	10	25	230	230	1500	250	1899	994	7.2	8.0
FS-85	160	80	8	25	140	60	1500	100	1220	466	6.4	3.0
FS-86	200	120	8	25	180	100	1500	100	1498	608	6.1	3.2
FS-87	220	140	8	25	200	120	1500	100	1635	675	8.6	2.5
FS-88	250	180	8	25	230	160	1500	100	1855	792	8.3	3.4
FS-89	160	80	8	25	140	60	1500	150	1220	464	7.1	2.8
FS-90	200	120	8	25	180	100	1500	150	1498	607	6.4	2.9
FS-91	220	140	8	25	200	120	1500	150	1635	686	6.4	2.9
FS-92	250	180	8	25	230	160	1500	150	1862	808	6.9	2.6
FS-93	160	80	8	25	140	60	1500	250	1209	469	6.1	2.5
FS-94	200	120	8	25	180	100	1500	250	1513	609	6.4	2.3
FS-95	220	140	8	25	200	120	1500	250	1651	685	7.9	4.1
FS-96	250	180	8	25	230	160	1500	250	1889	791	7.0	4.7
FS-97-t/100	200	200	8	25	180	180	1500	150	1991	834	3.2	5.1
FS-98-t/10	200	200	8	25	180	180	1500	150	1916	813	4.9	4.3
FS-99-t/5	200	200	8	25	180	180	1500	150	1860	771	7.8	3.1
FS-100-t/2	200	200	8	25	180	180	1500	150	1736	658	10.8	3.0
FS-101-t	200	200	8	25	180	180	1500	150	1594	524	15.7	2.2
FS-102-L/2000	200	200	8	25	180	180	1500	150	1920	815	5.2	2.5
FS-103-L/1500	200	200	8	25	180	180	1500	150	1901	803	5.3	4.0
FS-104-L/1000	200	200	8	25	180	180	1500	150	1867	776	7.1	2.1
FS-105-L/500	200	200	8	25	180	180	1500	150	1780	707	8.7	3.1
FS-106-D/20	200	200	8	25	180	180	1500	150	1808	733	8.4	2.1
FS-107-D/8	200	200	8	25	180	180	1500	150	1808	733	8.4	2.1
FS-108-D/4	200	200	8	25	180	180	1500	150	1808	733	8.4	2.1

t_t, L_t, d, b, P_u, Δ_u, K_e, and DI denote shear keys' thickness, height, length, width, tube's ultimate compressive resistance, axial shortening, initial stiffness, and ductility index, respectively.

4.2 Tubes design

As depicted in Figs. 1(a) and 7, the shear-keyed tube design was based on the authors' five-story corner-supported MSS office buildings designed under Chinese steel design code GB 50017-2017 [79]. The Haoshi office building was constructed with 68 modular units measuring 13.8×3.6×3.5 and 14.4×3.6×3.5 m. In contrast, two blocks of the Tianjin Ziya office building utilized 314 modules measuring 8.5×3.0×3.0 and 6.7×3.0×3.0 m. Additionally, each of these hybrid types of MSS consisted of two steel frame cores functioning as staircases to prevent lateral sway and IMC rotation, improving the buckling strength of columns [80]. The primary objective was to conduct extensive parametric and analytic studies; consequently, tube cross-sections were selected per the prototype project. The inflection point was established by designing the column height as half of the actual, as indicated in **Fig. 1(b)**, and tube height was designed using column subassembly, as recommended in Ref. [81]. In this investigation, the top and lower plates were connected by a box-shaped shear key [26]. Shear keys were inserted inside SHS tubes to replicate the actual scenario, and connecting plates were not welded to the tubes to allow movement. In order to account for fabrication tolerances, a gap of 2 mm between the tube and the shear-key was specified in the FE models, as reported in shear-keyed IMC [28,29] and post-tensioned frames [51,82] studies.

4.3 Tubes geometry

The geometrical details of the shear-keyed tube are depicted in **Fig. 7**. Since the purpose of the study was to determine the efficacy of shear keys, various parameters are designed according to **Table 4**. The standard L_c for shear-keyed tubes was determined to be 1.5 m, varying from 1.5 to 1.0, 1.2, 1.8, 2.4, 3.0, and 3.6 m. The case studies in **Fig. 1(a)** utilized tubular columns with a lower D/t_c and L_c/r_c ratio to improve their slenderness and stability, avoid flexural buckling and ensure a 50-year design life of MSS against 8-degree seismic forces. Therefore, D, B, and t_c of the tube's cross-section varied from 200×200×8 to 200×200×5, 200×200×7, 200×200×9, 200×200×10, 150×150×10, 180×180×10, 220×220×10, 250×250×10, 160×80×8, 200×120×8, 220×140×8, and 250×180×8 mm. In comparison, the size of the connecting plate remained constant, measuring 524×484×20 mm.

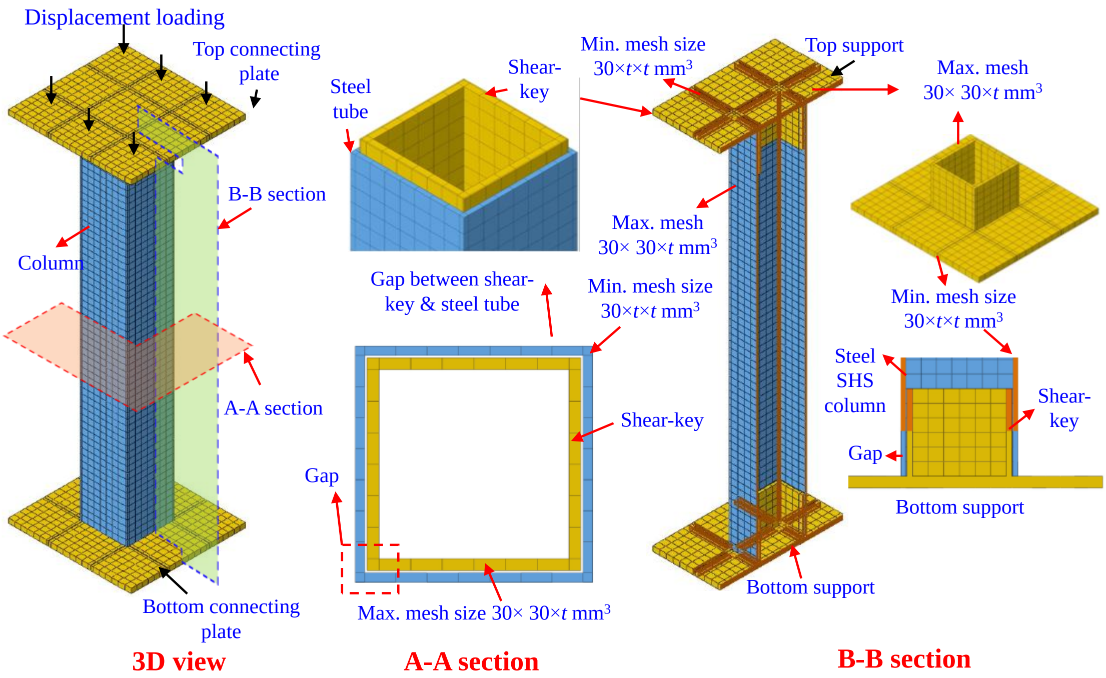

Fig. 7 Developed FEM of shear-keyed tubes

4.4 Tubes developed FEM

The FEM depicted in **Fig. 7** consists of shear keys welded to connecting plates, steel tubes, and connecting plates. Since the hot-rolled section is used in the prototype project, all components meshed with C3D8R elements following the Refs. [28,29] on shear-keyed frames and Refs. [58] and [12,13] on tubular walls. All corners around the tube or shear key cross-section thickness were partitioned to form the structured mesh. Corners have smaller element sizes than other regions, suggesting a minimum mesh size of $30 \times t \times t$ (mm^3). The uniform mesh was applied to other regions; therefore, they had bigger element sizes than corners, providing them a maximum mesh size of $30 \times 30 \times t$ (mm^3).

Upper and lower connecting plates are always flat, so their movement in each direction was constrained. To permit vertical displacement, the bottom section was allowed to move vertically. Surface-based kinematic coupling constraints were attained by defining the reference nodes on the centers of the lower and upper connecting plates and restraining all degrees of freedom at the coupling nodes. Connecting plates and shear keys established surface-to-surface contact with ties to fuse them and constrain their relative motion. The column's interaction with the connecting plates and shear keys was represented as surface-to-surface (standard), using "hard contact" as the normal behavior and "penalty friction formulation" as tangential with a friction coefficient of 0.3. On the other hand, the "no key" model assumed a tube welded to the plates, achieved by the surface-to-surface tie constraint. Q345 was employed in the shear-keyed tube design of the authors' prototype project since it is often used in the Chinese industry. Similarly, according to ASTPM, Q345 is substituted for S355, as their strength, stiffness, and ductility are nearly identical [83]. Consequently, the yield and ultimate strengths of 380 and 503 MPa for the shear-keyed tubes were obtained by averaging the values of specimens made of S355, i.e.,140×80×4, 140×80×6, 160×80×5, 200×80×10 listed in **Table 2** from AS19-AS22 as reported in Refs. [12–14,58]. The modulus of elasticity was determined to be 206 GPa. These values were used to maintain consistency with the MSS shear-keyed building design.

When imperfection is related to the first buckling mode, the bifurcation point closely resembles the first eigenvalue estimated for the ideal structure [84]. According to Ref. [62], the first eigenmode is more significant and is considered the most crucial in elastic buckling, so it is introduced and scaled as the structure's initial defect. Another study on IMC's axial compression behavior in MSS used the first mode to input imperfection amplitude [10]. According to validated test sources in Refs. [56,57], tests on MSB's

IMC in Ref. [10], and numerical studies in Ref. [84] and [62], imperfection application in the first buckling mode is a reliable, critical, and extensively employed approach. This study used the lowest buckling mode for initial geometric imperfections to acquire reliable outcomes. The initial geometric imperfection of tubular walls was obtained $L_c/600$ by comparing the load-shortening curves of FE to those of tests reported by Hou et al. [58] and Khan et al. [12,13]. Thus, shear-keyed tubes that were built as hot-rolled sections used a magnitude of $L_c/600$ to perform the parametric study.

4.5 Typical load-shortening behavior

Generalized load-shortening curves are depicted in **Fig. 8**, illustrating the existence of linear elastic (I), nonlinear (II), and recession (III) zones for type A and B curves. The recession is a state of the load-shortening curves after the ultimate/peak stage with a subsequent trough characterized by a significant drop in the tubes' load-carrying capacity that can persist to larger end-shortening values. This is specified as post-ultimate or post-peak dropping or falling branches, consistent in Refs. [85–91]. The figure indicates that load increases linearly during the initial linear state with shortening till yield stage P_y. It implies that type A FEMs had a shorter elastic branch and yielded sooner than type B. This shortening could be caused by the decreased compression strength of shear-keyed tubes, reducing yield and ultimate strengths. The stiffness reduction of curves started at P_y because stresses on the several locations on tubes exceeded the material yield strength. Following P_y until P_u, the curves have a parabolic shape; at the same time, local buckling becomes apparent as the tube reaches compression capacity. Shear-keyed columns undergo local plastic buckling after stage II. In contrast to stage I, stage II of type A curve FEM is more prolonged than type B, illustrating the superior ductility of type A FEMs. This is evident from **Table 4**. This is because increasing the rigidity or decreasing the slenderness with thicker or shorter tubes or longer and thicker shear-key improves compressive strength but impairs ductility. During stage II, the tube attains P_u and undergoes local inward or outward buckling. Stage III is characterized by a decrease in the load that the tube can support (load-carrying capacity) and significant local buckling. Similarly, at the post-ultimate stage, the *DI* can be compared. The capacity of type B FEMs is noticeably lower than that of type A, indicating that tubes cannot offer resistance after buckling has been initiated.

Shear-keyed tubes have varying flexural stiffness on ends and mid that generate non-homogeneity and non-uniform stress distribution [92]. This reduces end rotational stiffness, increases slenderness, and weakens shear-keyed tubes relative to tubes without shear keys [80]. Besides, semi-rigid shear keys with low tube-end stiffnesses generate stresses in columns subjected to axial compression, resulting in yield and ultimate capacity reductions [35]. This weakening effect on tubes is consistent with Refs. [12–14,58]. Shear stresses in columns are increased in tubes with non-welded shear keys compared to tubes without shear keys, and compressive behavior is degraded. The shear keys transmit shear forces till considerable tube deformation, with force increasing as the tube deforms [93]. Neglecting shear stresses or assuming welding of shear-keyed IMC to tubes would overestimate buckling strength [94].

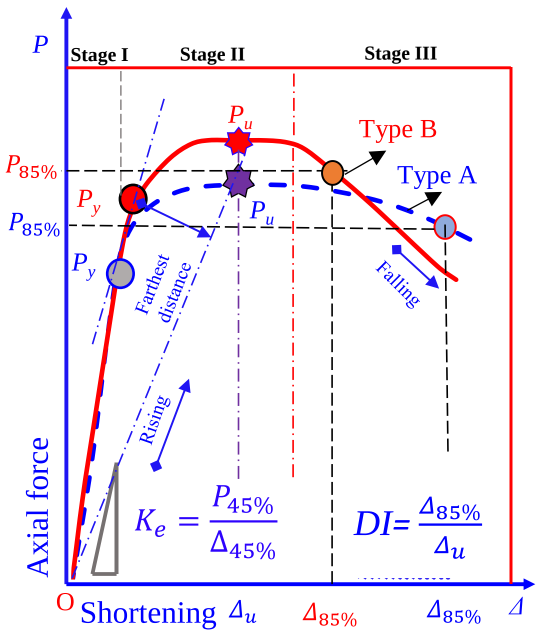

Fig. 8 Typical compressive behavior of shear-keyed tubes

4.6 Typical failure modes

Supplementary Fig. B1 organizes the failure modes of all 109 FEMs from No key to FS-108. Moreover, **Fig. 9(a-f)** summarizes graphs that gather similar column behavior per parametric studies in **Table 4**. Comparing tubes with and without shear keys reveals that tubes without shear-keyed IMC failed with IB or OB, whereas shear-keyed tubes faced sinusoidal IB and OB, the same on opposite and opposite on adjacent faces. This failure was more visible in short columns than in long tubes. Long or rectangular tubes with substantially higher cross-section lengths than widths display stress localization near the loading end; thus, failure starts on shear-key edges in the longer direction and spreads to the shorter side. This is because the longer side has a lower flexural stiffness. If the buckling resistance of tubes is considerably raised by increasing the shear-key height and thickness and total stiffness of the column, the failure mode extends away from the edges, and the behavior becomes uniform. Additionally, the influence of varying imperfection values on failure behavior was not evident; however, load-shortening curves seem extremely sensitive.

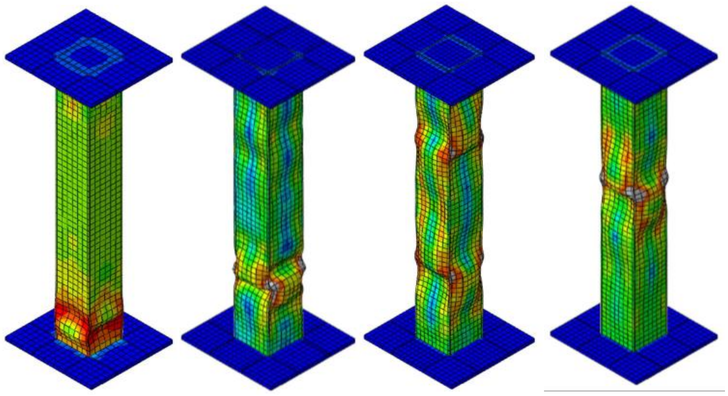

(a) Effect of shear-key thickness (t_t)

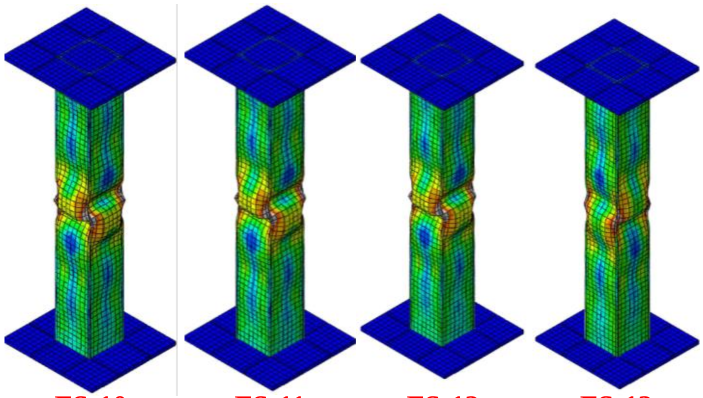

(b) Effect of shear-key height (L_t)

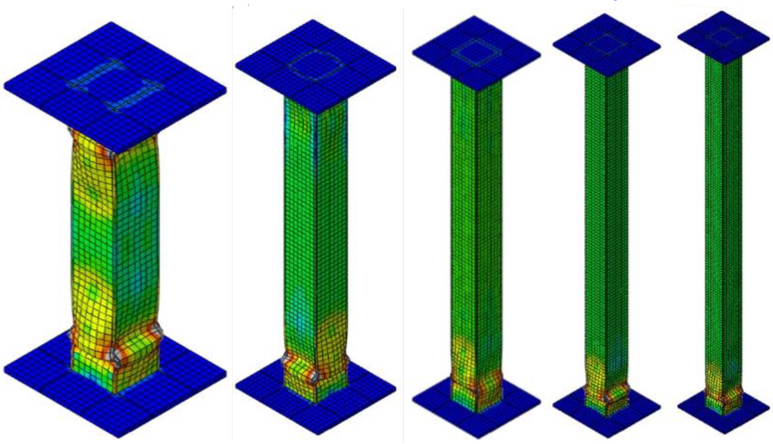

(c) Effect of tube height (L_c)

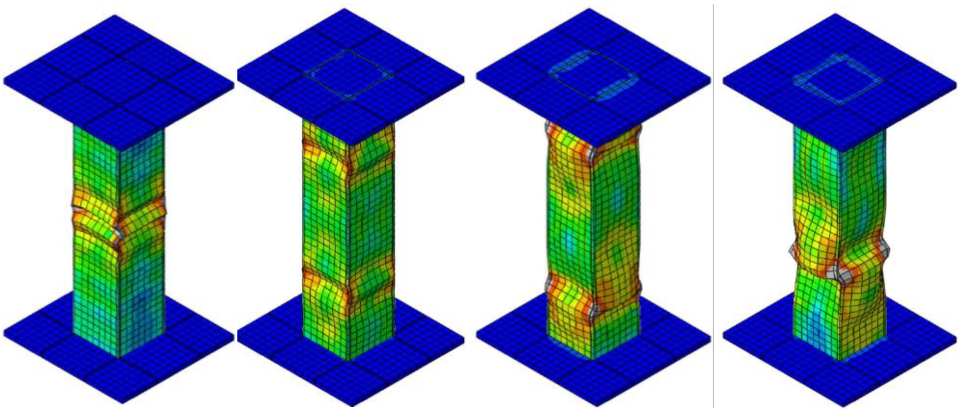

(d) Effect of tube thickness (t_c)

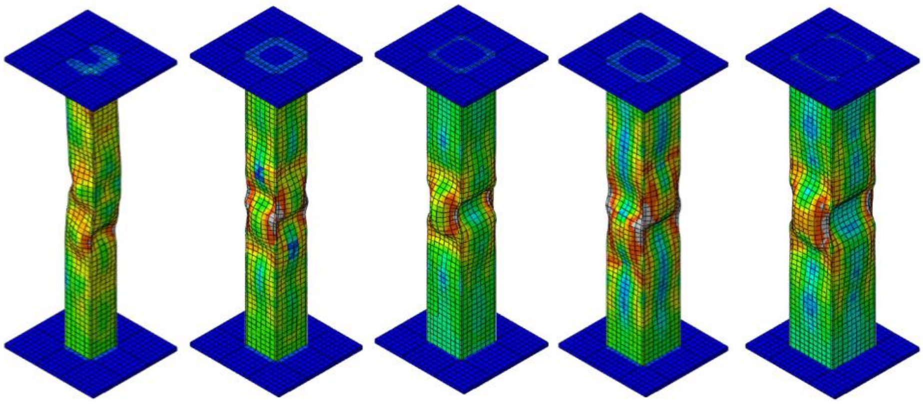

(e) Effect of tube $D \times B$

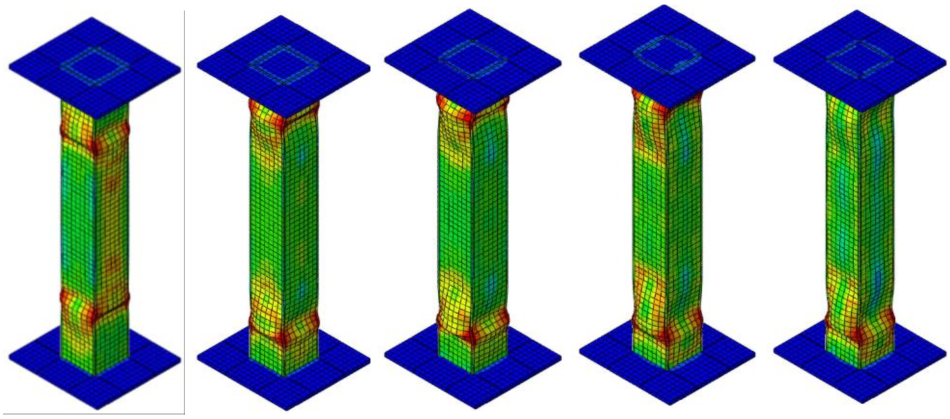

(f) Effect of imperfection

Fig. 9 Shear-keyed tubes' typical failure modes

4.7 Discussions using parametric analysis

4.7.1 Shear-key thickness effects (t_t)

Figure 10(a-c) illustrates the influence of the t_t (i.e., 15, 20, and 25 mm) on the *P-Δ* curves. The effect on the P_u, K_e, Δ_u, and *DI* ratios with varied L_t (i.e., 100, 150, and 250 mm) is shown in **Fig. 11(a-d)**. Raising t_t has beneficial effects on P_u and K_e but shows a weaker relationship and has a significant variation on Δ_u. As the t_t rises from 15 to 20 and 25 mm, the P_u (K_e) improves by 11% to 51% (14% to 32%) with 100 mm L_t. Increasing the t_t reduces slenderness and raises compressive resistance. Furthermore, altering t_t had a varying effect on *DI* ratios due to obvious scatters except with 250 mm L_t. Moreover, the impact on Δ_u showed an inconsistent relationship, such as unfavorable, with falls for 100 mm and favorable with rise for 150 mm L_t. Because increased shear-keyed IMC stiffness causes plastic buckling/yielding. This improves tube yield strength while reducing buckling strain, hence impairing Δ_u. Comparing tubes with and without shear keys in **Fig. 10** and **Table 4** reveals that shear-keyed tubes reduce P_u and K_e. It is because the presence of non-welded shear-keyed IMC affects rotational stiffness and slenderness and produces stresses in columns, resulting in yield and ultimate capacity reductions, as Refs. [35], [92], [80], [93], and [94].

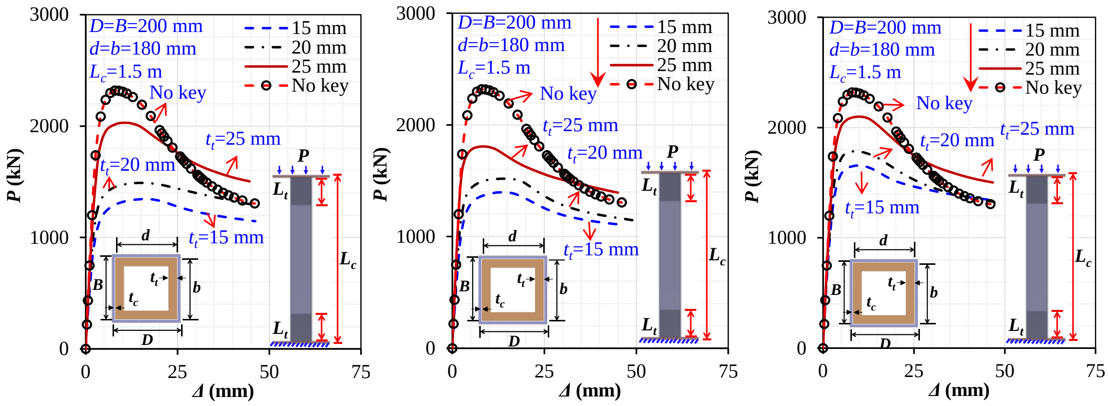

(a) L_t=100 mm (b) L_t=150 mm (c) L_t=250 mm

Fig. 10 Effect of t_t on *P*-Δ curves for given L_t

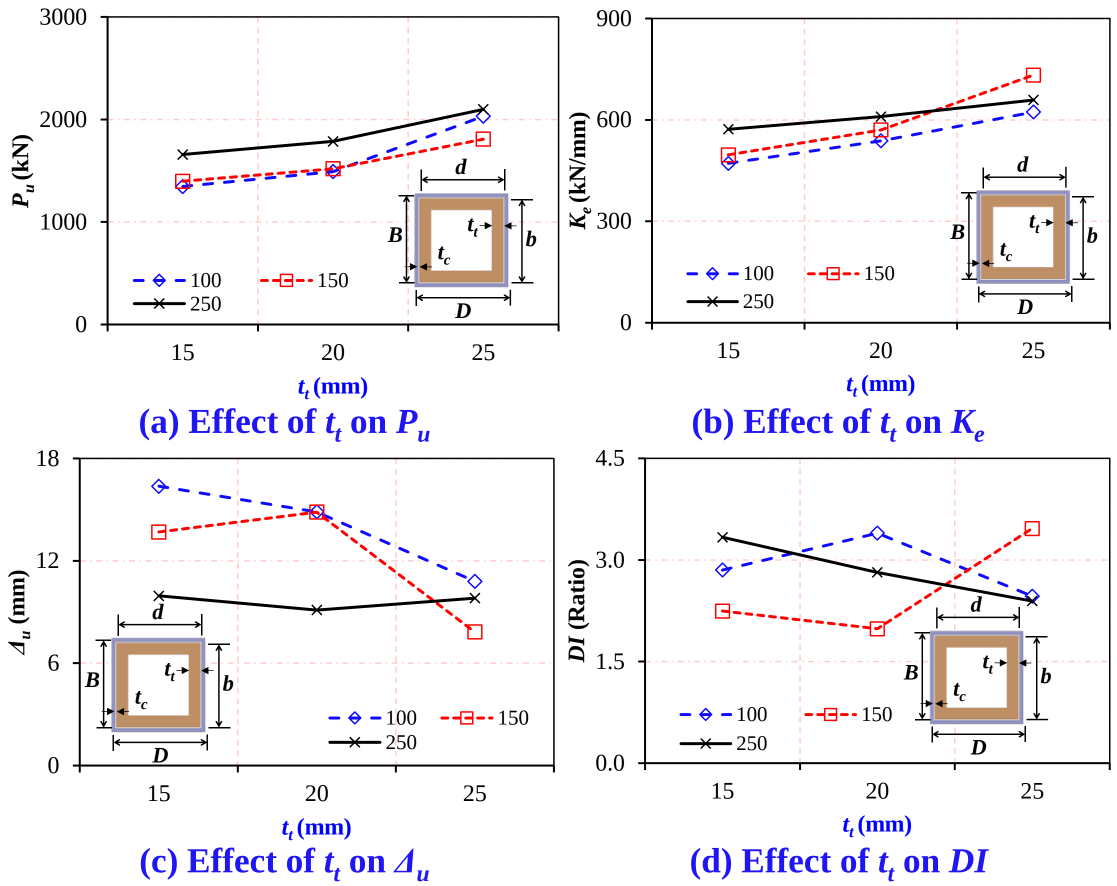

Fig. 11 Effect of t_t on P_u, K_e, Δ_u, and DI

4.7.2 Shear-key height effects (L_t)

Figure 12(a-d) demonstrates the L_t (i.e., 75, 150, 250, and 300 mm) impact on P-Δ curves. **Figure 15(a-d)** illustrates a variation in P_u, K_e, Δ_u, and DI ratios with various t_t (15, 20, 25, and 35 mm). Raising L_t has a minor effect on P_u (K_e) upto 5% (2%) but a noticeable detrimental effect on Δ_u. This impact is more apparent when a larger value of t_t is used. Increasing the L_t improves compressive resistance due to the enlargement of shear keys, making a tube-connecting plate joint stiffer. Furthermore, modifying L_t possessed a weaker relationship with the DI, yet, the impact with thicker keys was noteworthy because longer and thicker shear keys extend the recession stage. The rise of L_t *is* weakly related to Δ_u. Increasing shear-key length improves tube yield strength while reducing buckling strain, which influences ductility. **Figure 12** and **Table 4** show that the shear keys significantly reduce tubes P_u (K_e) up to 42% (30%) for t_t of 15 mm compared to tubes without shear keys; nevertheless, the drop in percentage rise is evident with larger shear keys due to their improved compressive behavior.

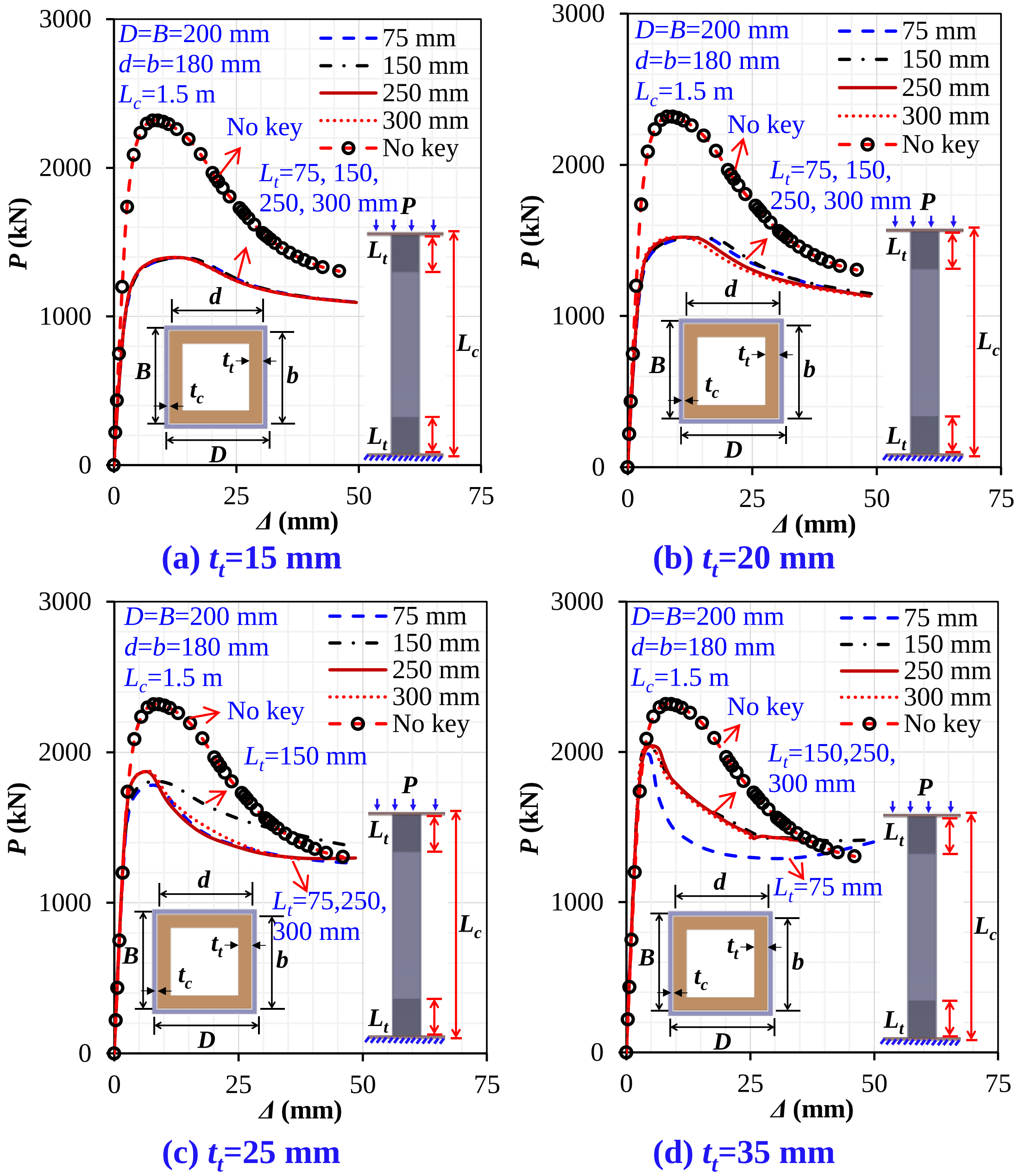

Fig. 12 Influence of L_t on P-Δ curves for given t_t

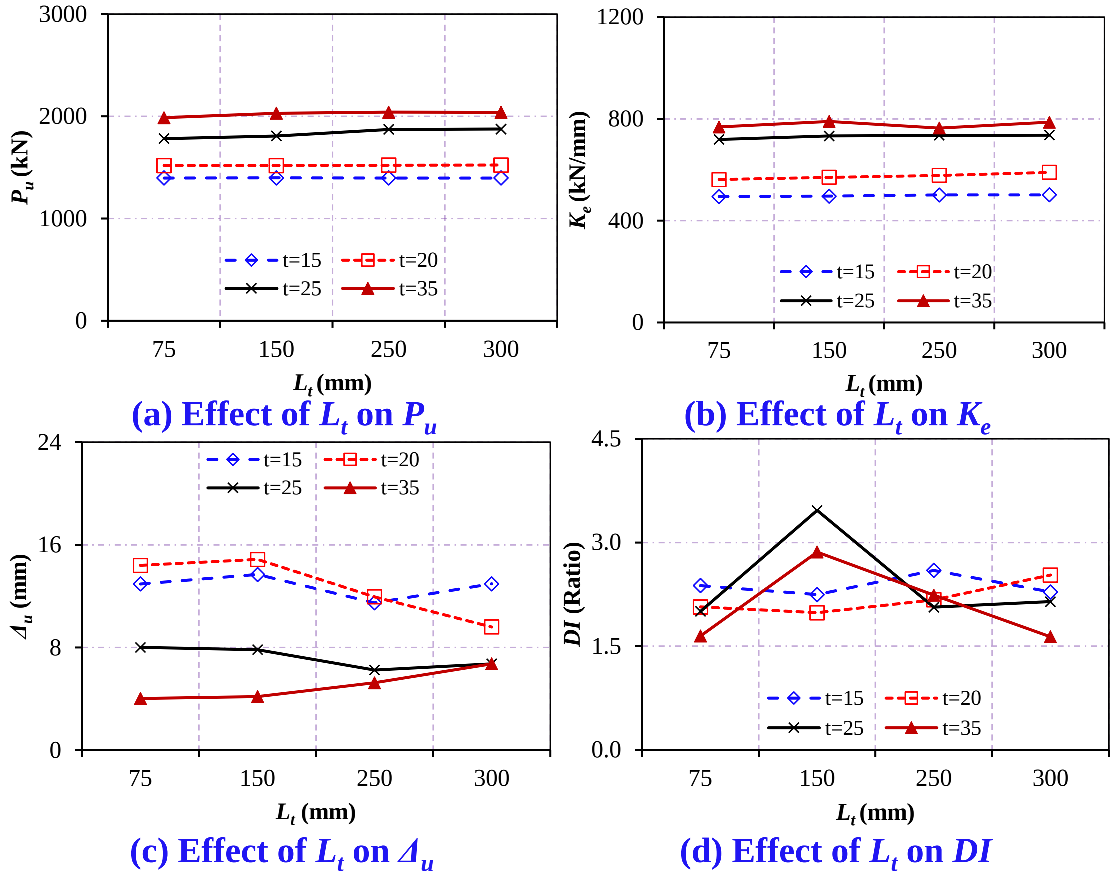

Fig. 13 Influence of L_t on P_u, K_e, Δ_u, and DI

4.7.3 Column's height (L_c)

Figure 14(a-d) displays the effect of L_c (i.e., 1.2, 1.8, 2.4, 3.0, and 3.6 m) on the P-Δ graphs. **Figure 15(a-d)** summarizes the variation trend of P_u, K_e, Δ_u, and DI ratios with varying L_t (i.e., 75, 150, 250, and 300 mm). Growing L_c showed no noticeable influence on P_u while linearly reducing K_e and DI. Raising L_c decreased K_e upto 61% by increasing the L_c/r ratio, making the column more susceptible to the shear-keyed IMC's shear effect. Besides, tube-key boundary interactions also become weaker.

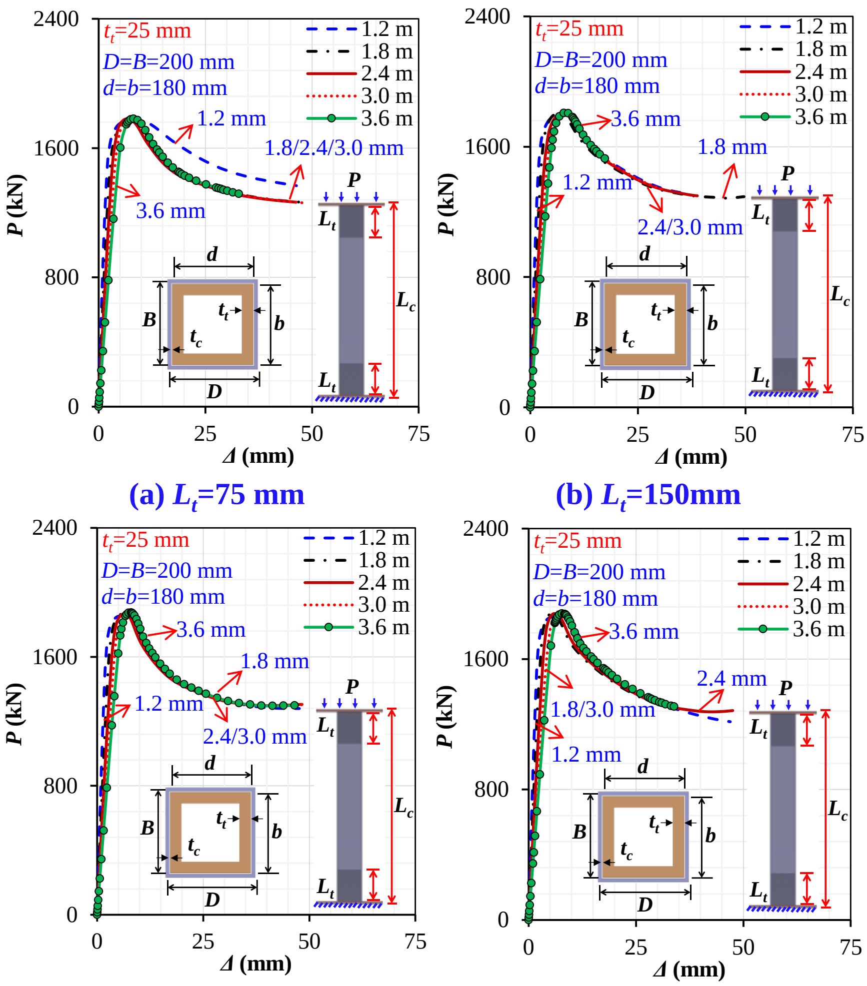

(a) L_t=75 mm (b) L_t=150mm

(c) L_t=250 mm (d) L_t=300 mm

Fig. 14 Impact of the L_c on P-Δ curves for given L_t

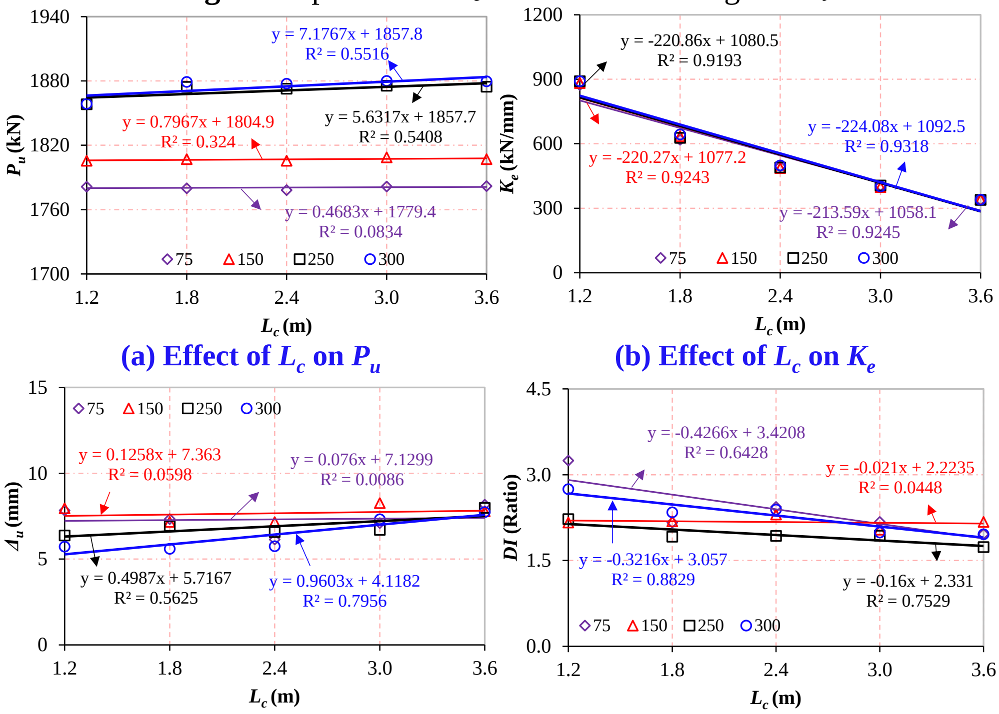

(a) Effect of L_c on P_u (b) Effect of L_c on K_e

(c) Effect of L_c on Δ_u (d) Effect of L_c on DI

Fig. 15 Impact of the L_c on P_u, K_e, Δ_u, and DI

4.7.4 Column's thickness (t_c)

The effects of varying t_c (i.e., 5, 7, 8, and 9 mm) for given L_c (i.e., 1 and 3 m) and L_t (i.e., 100, 150, and 250 mm) on the *P-Δ* graphs are depicted in **Fig. 16(a,b)**. **Figure 16(c,d)** plots the varying trends of P_u, K_e, Δu, and *DI* ratios. It demonstrates a linear rise in P_u and K_e as the t_c improves. For the 3 m L_c, the P_u (K_e) increased upto 135% (207%) and 129% (147%) for the L_c of 1 m. Simultaneously, *DI* shows a weaker relationship; while Δ_u is fallen for 3 m L_c columns. However, *DI* shows a larger scatter, and Δ_u has risen for 1 m L_c columns. Increasing t_c decreases cross-sectional slenderness (D/t_c), or L_c/r, which improves buckling resistances of columns, thereby enhancing the tubes' strength and stiffness. Compared to short tubes, tubes with a larger L_c exhibit a decrease in ductility due to higher member slenderness, which makes the column more susceptible to non-uniform stress distribution, localization, and non-yielding due to the shear keys' apparent shear effect. Moreover, D/t_c falls from 40 to 22, as t_c rises from 5 to 9 mm, changing the cross-section from Class 4 to 1.

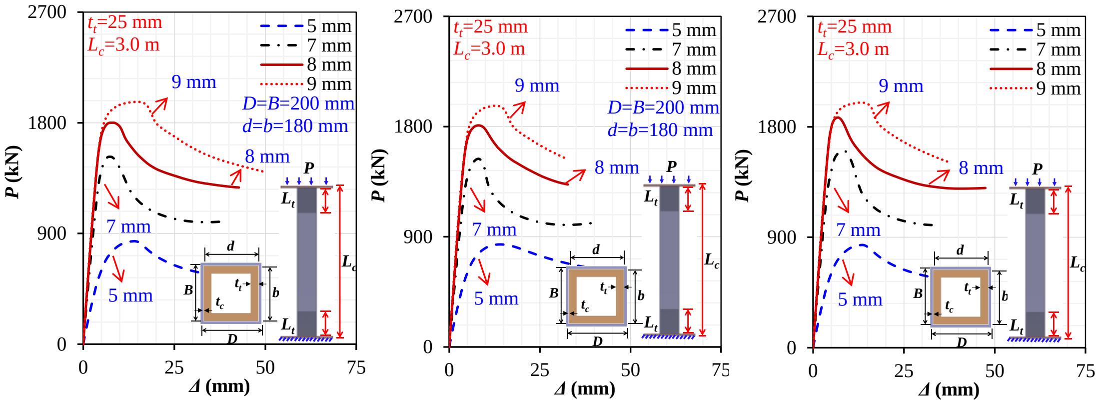

L_t=100 mm L_t=150 mm L_t=250 mm

(a) Long shear-keyed tubular columns

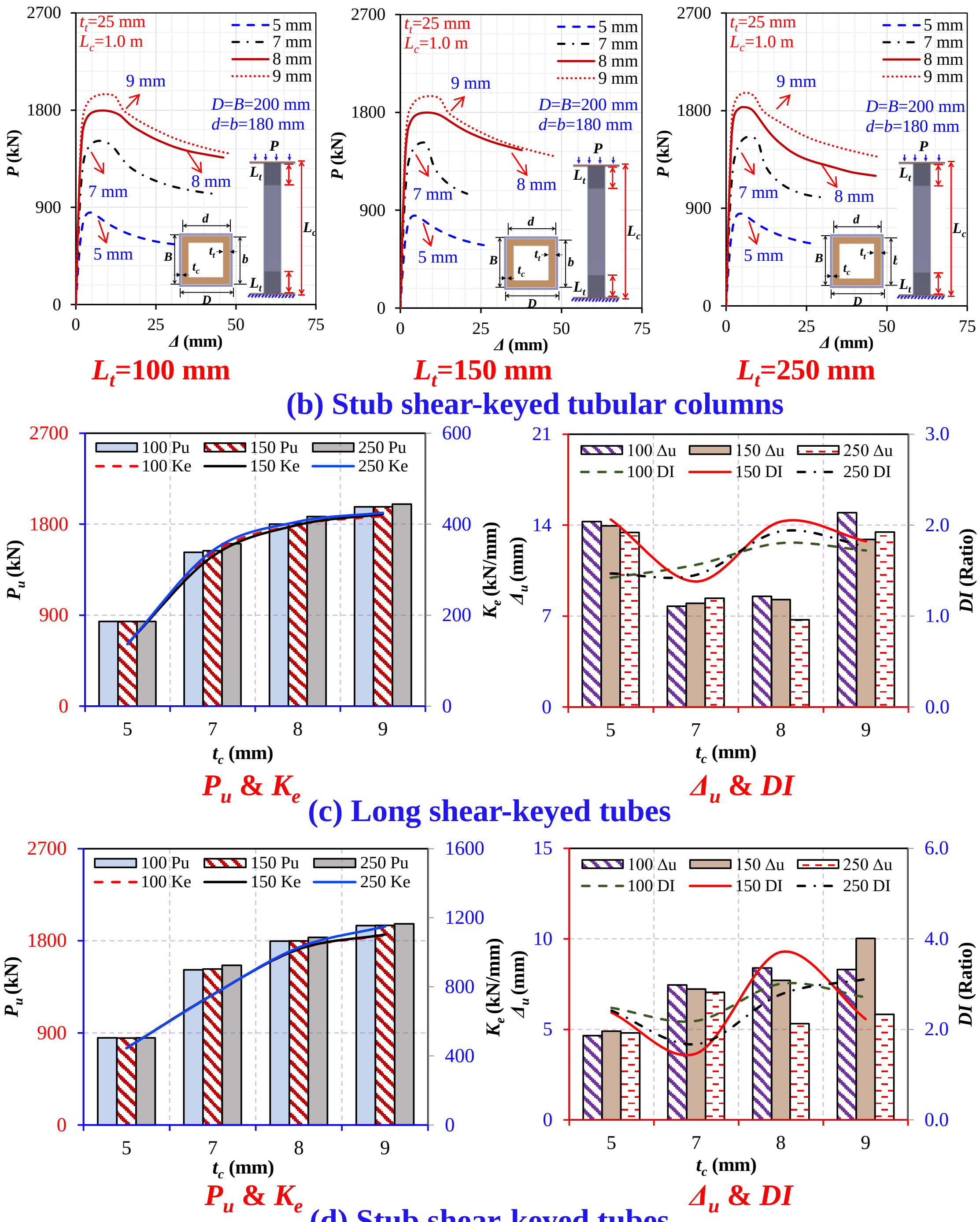

Fig. 16 Effect of t_c on P-Δ, P_u, K_e, Δ_u, and DI relationships

4.7.5 Tube cross-section (D×B)

Figure 17(a-d) depicts the outcome of modifying D and B with different L_t of 100, 150, and 250 mm. It demonstrates that as the D and B increase from 150 to 180, 200, 220, and 250 mm, P_u (K_e) increases linearly upto 8% (78%). Similarly, a 52% (70%) rise is noticed with enhancing B/D to 80/60, 120/200, 140/220, and 180/250 mm. This is so that buckling resistances can be improved by raising D and B, which also decreases slenderness. Simultaneously, square tubes Δ_u showed a decrement of upto 56%, whereas DI increased by upto 140%. It is because a larger cross-section undergoes yielding, decreasing buckling strain but prolonging recession behavior. On the contrary, rectangular tubes Δ_u and DI showed a weaker relationship with an increase or decrease in D or B. This might be due to varying non-uniform stress localization on shear keys on the longer side that could lead to premature buckling. Also, D/t_c increases from 15 to 18, 20, and 25 when D/B is increased from 150/150 to 180/180, 200/180, 220/220, and 250/250 mm with a t_c of 10 mm. The cross-section class changes when D/B increases from 160/80 to 200/120, 220/140, and 250/180 with 8 mm t_c, raising D/t_c increases from 20 to 25, 27, and 31.

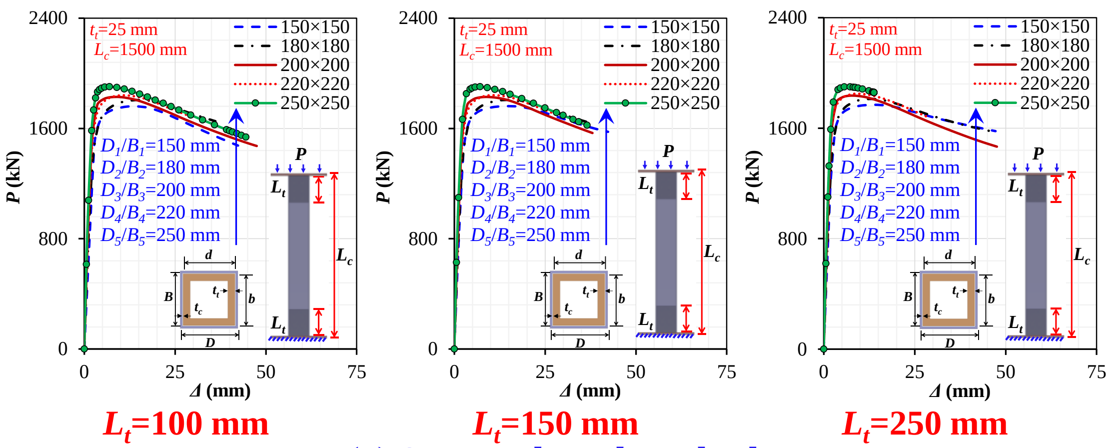

(a) Square shear-keyed tubes

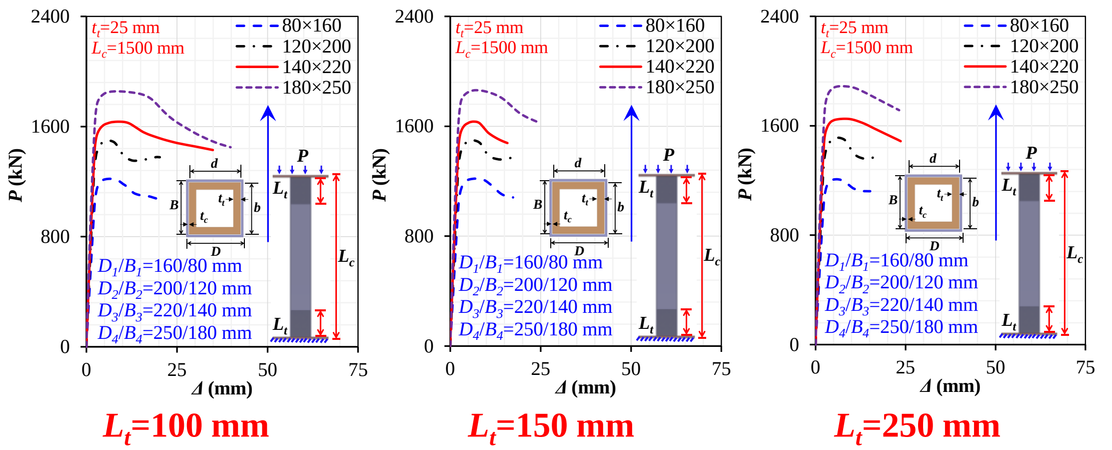

(b) Rectangular shear-keyed tubes

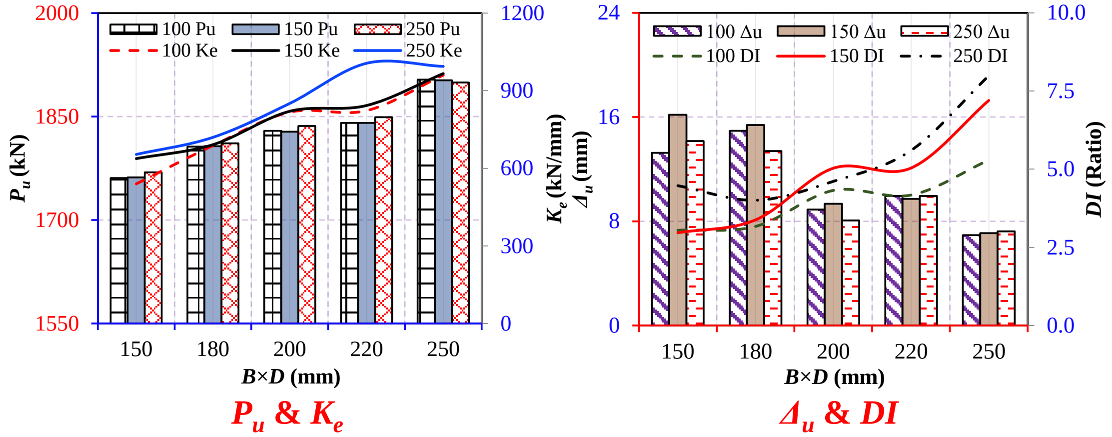

(c) Square shear-keyed tubes

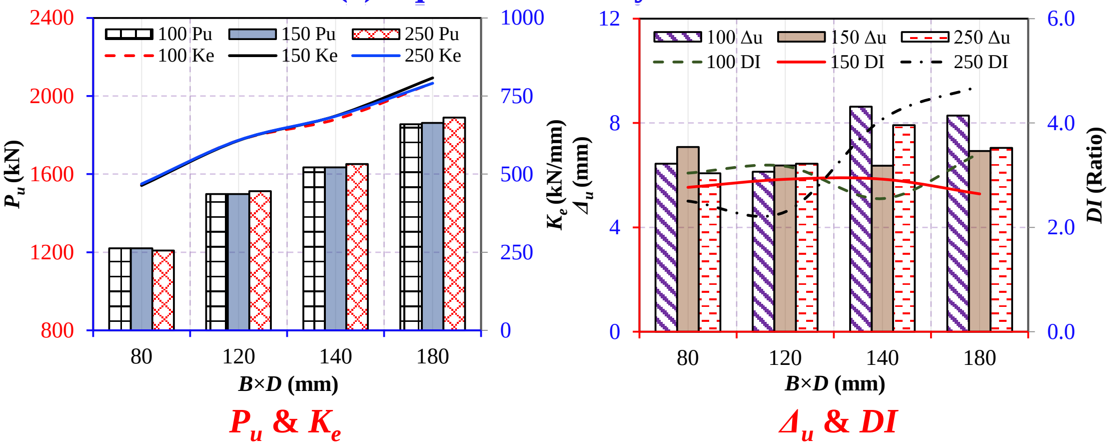

(d) Rectangular shear-keyed tubes

Fig. 17 Influence of $D \times B$ on P-Δ, P_u, K_e, Δ_u, and DI relationships

4.7.6 Initial imperfection

Compared to TSS, initial geometric imperfection on the shear-keyed tubes influences manufacturing, installing, and assembling MSS due to offsite fabrication and onsite installation flaws, impacting performance [10]. Given that the shear-keyed module column primarily transfers the structural loads to IMC, the initial imperfections issue is crucial for corner-supported MSS and has significant concerns [95]. Consequently, the parametric study explores shear-keyed tube compression behaviors for excessive initial imperfections as per Ref. [10]. Theofanous and Gardner [57] proposed that member thickness (t_c) or height (L_c) and applied eccentricity (e) contribute to local and global imperfections. This research chose imperfection values as tube thickness (t_c) of $t_c/100$, $t_c/10$, $t_c/5$, $t_c/2$, and t_c; tube height (L_c) of $L_c/2000$, $L_c/15000$, $L_c/1000$, and $L_c/500$; and eccentricity (e) of D/20, D/8, and D/4, and compared with the validated FE outcomes that used an initial magnitude of L_c/600. **Figure 18(a-c)** summarizes the influences on P-Δ graphs, whereas **Fig. 19(a-f)** shows variation in P_u, K_e, Δ_u, and DI trends. Increasing value from t_c/100 to t_c/10, t_c/5, t_c/2, and t_c lowered P_u (K_e) by upto 20% (37%). Compared to L_c/600, t_c/100, t_c/10, and t_c/5 overestimated P_u (K_e) by upto 10% (14%), while t_c/2 and t_c underestimated by upto 12% (28%). Whereas increasing from L_c/2000 to L_c/1500, L_c/1000, and L_c/500 dropped P_u (K_e) by upto 7% (13%). Moreover, L_c/2000 to L_c/1500 and L_c/1000 overestimated P_u (K_e) by upto 6% (11%), while L_c/500 was underestimated by 1% (3%) compared to L_c/600. Additionally, increasing from t_c/100 to t_c/10, t_c/5, t_c/2, and t_c raised Δ_u by upto 385% but decreased DI upto 57%. While rising from L_c/2000 to L_c/1500, L_c/1000, and L_c/500 lowered Δ_u (DI) upto 69% (26%). Compared to L_c/600, t_c/100 and t_c/10 overestimated Δ_u and underestimated DI, while t_c/2 and t_c underestimated Δ_u and overestimated DI. Likewise, L_c/2000, L_c/1500, and L_c/1000 overestimated Δ_u and DI, but L_c/500 underestimated Δ_u. This is because geometric imperfection accounts for secondary structural behavior, leading to significant strength and stiffness degradation [57,96]. Furthermore, the rising e from D/20 to D/8 and D/4 showed a non-apparent influence due to flat platens. Compared to the FE findings on shear-keyed tubes, the initial imperfection of L_c/500 is the closest indicator of actual compression behavior obtained by L_c/600 in the referenced study. Simultaneously, t_c/5 and L_c/1000 overestimated, while t_c/2 and L_c/500 underestimated it.

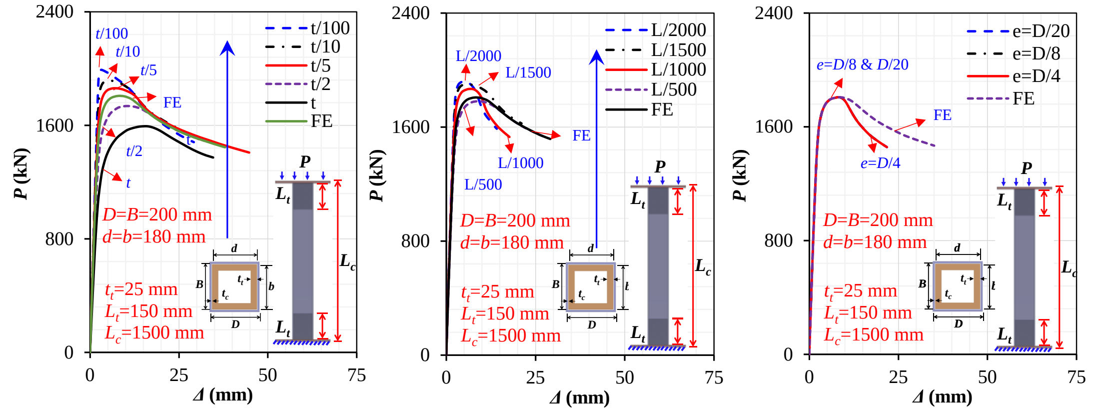

(a) Local imperfection t_c (b) Local imperfection L_c (c) Geometric imperfection e

Fig. 18 Influence of initial imperfection P-$\varDelta$ curves

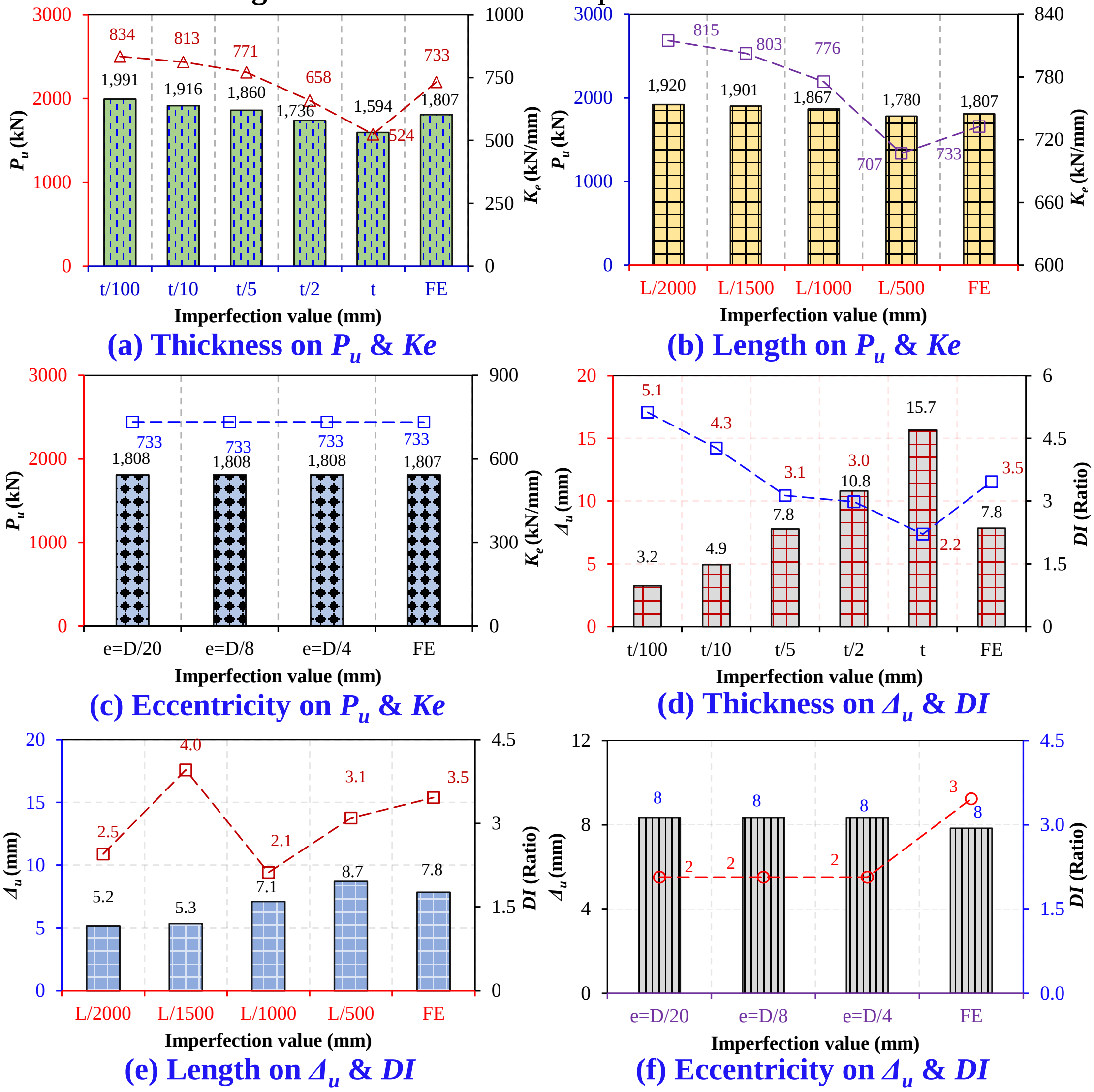

(a) Thickness on P_u & Ke (b) Length on P_u & Ke

(c) Eccentricity on P_u & Ke (d) Thickness on $\varDelta_u$ & DI

(e) Length on $\varDelta_u$ & DI (f) Eccentricity on $\varDelta_u$ & DI

Fig. 19 Influence of initial imperfection on P_u, K_e, $\varDelta_u$, and DI relationships

5 Analytical research on ultimate resistance predictions using design standards

The approach presented in **Fig. 20** has been widely utilized in Ref. [97], [57], and [98] to evaluate the applicability of design standard prediction equations. In EC3 [99], members' cross-sectional ($P_{u,c}$) and buckling ($P_{u,b}$) resistance via Eqns. 5~7, representing EC3-C and EC3-B, are used to design shear-keyed tubes:

$$P_{u,c} = f_y A_s(\text{or } A_{eff})\,/\gamma_M\ ;\ P_{u,b} = \chi f_y A_s(\text{or } A_{eff})\,/\gamma_M \tag{5}$$

$$\chi = 1/[\phi + (\phi^2 - \bar{\lambda}^2)^{0.5}] \leq 1 \tag{6}$$

$$\phi = 0.5\left[1 + \alpha\left(\bar{\lambda} - 0.2\right) + \bar{\lambda}^2\right];\ \bar{\lambda} = \sqrt{f_y A_s / P_{cr}} \tag{7}$$

where P_{cr} and γ_M represent critical load [100] and a partial safety factor. The code [101,102], standards [103], statistical studies [104], and research [12–14] recommend 1.0, overestimating 101 and 98 outcomes for $P_{u,c}$ and $P_{u,b}$.

An analogous procedure has been used to draw the results with CSA S16-19 [105] and AISC360-16 [106] that adopt a resistance factor of 0.90 [107], overestimating 90 and 96 outcomes. Similarly, the GB50017-2017 standard [79] overestimates 104 results, with $\alpha_1, \alpha_2,$ and α_3 of 0.65, 0.965, and 0.3.

5.1 Validations

The applicability of EC3-C, EC3-B, CSA S16, AISC360-16, and GB50017-2017 was examined by comparing analysis-to-prediction ratios of shear-keyed tubes P_u summarized in **Table 4**. Cross-sectional ($P_{u,c}$) and buckling ($P_{u,b}$) resistances in EC3:1-1 are represented as EC3-C and EC3-B. **Figure 20** demonstrates that conventional design standards provide non-conservative outcomes with 101, 98, 90, 96, and 104 over- and 6, 9, 17, 11, and 3 under-estimations. Due to underestimating the strength, slender cross-sections generally yielded conservative results. Thus, strength reduction factors modifications as a function of the shear-keyed IMC and tube parameters are required to accurately anticipate the shear-keyed tubes' compressive behavior.

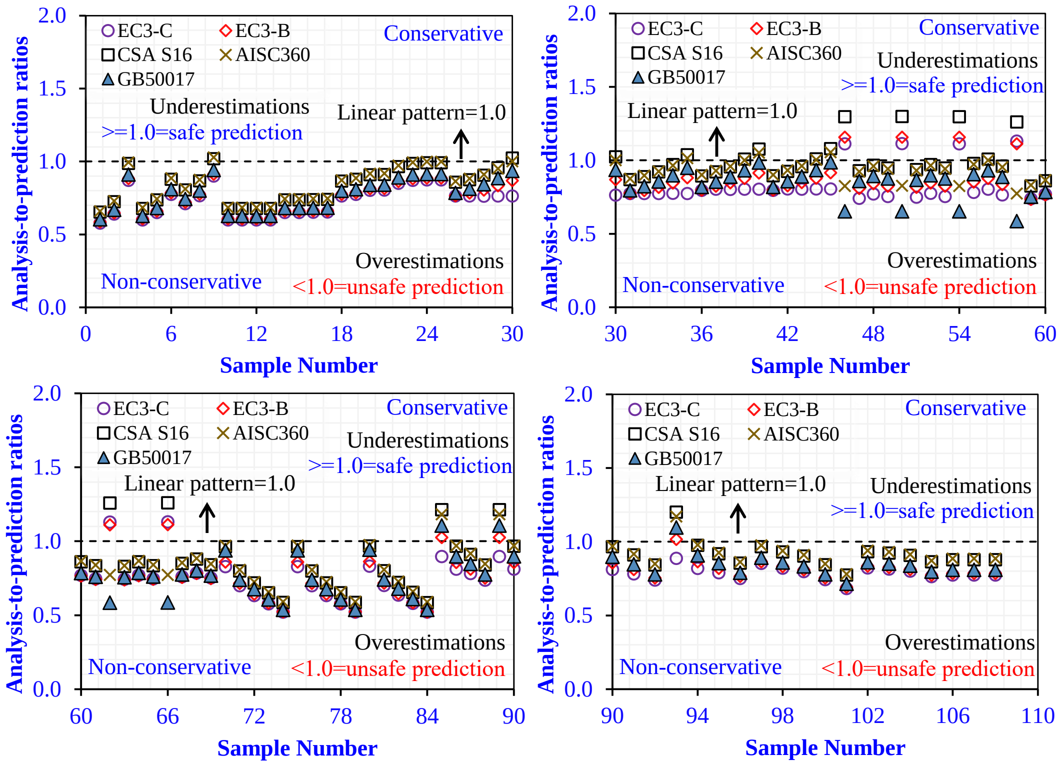

Sample No	1-30		30-60		60-90		90-108		Total	
	Mean	Cov	Mean	Cov	Mean	Cov	Mean	Cov	Mean	Cov
○ EC3-C	0.73	0.14	0.82	0.14	0.74	0.20	0.79	0.06	0.77	0.16
◇ EC3-B	0.75	0.14	0.87	0.13	0.76	0.21	0.82	0.08	0.80	0.16
□ CSA S16	0.84	0.15	1.00	0.13	0.86	0.22	0.92	0.10	0.90	0.17
✖ AISC360	0.84	0.14	0.93	0.07	0.83	0.18	0.92	0.09	0.87	0.14
▲ GB50017	0.77	0.15	0.85	0.12	0.76	0.20	0.85	0.10	0.80	0.15

Fig. 20 Non-modified prediction equations outcomes

6 Conclusions

This research examined shear-keyed columns' compression behaviors by evaluating the parametric effect using validated FEM. The compression resistances were estimated using conventional design standards prediction equations. This study supports the following outcomes:

1. The shear-keyed columns' load-shortening behavior reveals better compressive behavior accompanied by weaker ductility with larger shear-keyed IMC (greater t_t and L_t) and vice versa. Local buckling initiates when tubes achieve their ultimate compressive strength, causing their capacity to decline.

2. Buckling at ends is observed in long or rectangular tubes with shorter shear-key due to stress localization, whereas stub or intermediate tubes with longer shear-key shift it away from the column's ends. Local inward buckling accompanied outward, producing a sinusoidal pattern opposite on neighboring and similar on opposite faces.
3. Raising tubes and shear-key stiffening parameters increases strength and stiffness while increasing member length or slenderness ratio reduces stiffness and ductility. Longer tubes with a slender shear-key exhibit a more decrease in ductility due to slenderness or shear-key shear stresses. Capacity and stiffness dropped by raising imperfection from t_c/100 to t_c /10, t_c /5, t_c /2, and t_c, and L_c/2000 to L_c/1500, L_c/1000, and L_c/500. Increasing t_c/100 to t_c raised Δ_u but lowered *DI*, whereas increasing L_c/2000 to L_c/500 reduced Δ_u and *DI*.
4. Due to shear-key influence, the capacity decreases significantly, making it challenging to achieve conservative outcomes with conventional design standards, necessitating more restrictive resistance factors based on the tube and shear-keyed IMC parameters.

This study focused primarily on the parametric compression behaviors of single shear-keyed tubular columns. Thus, findings are restricted to the examined models. Based on experimental, numerical, and analytical assessments, future studies will be conducted on group shear-keyed columns, i.e., four neighboring module columns, which will be more appropriate to the practical development of MSS.

Acknowledgment

The authors gratefully acknowledge financial support from the National Natural Science Foundation of China (Grant Nos. 51978457 and 52008292) and the China Scholarship Council. The authors appreciate the editors' and reviewers' efforts in providing valuable recommendations that helped us improve the quality of the manuscript.

References

[1] Z. Chen, K. Khan, A. Khan, K. Javed, J. Liu, Exploration of the multidirectional stability and response of prefabricated volumetric modular steel structures, J. Constr. Steel Res. 184 (2021) 106826. https://doi.org/10.1016/j.jcsr.2021.106826.

[2] K. Khan, Z. Chen, J. Liu, K. Javed, State-of-the-Art on Technological Developments and Adaptability of Prefabricated Industrial Steel Buildings, Appl. Sci. 13 (2023).

[3] R.M. Lawson, Building design using modules, Steel Constr. Inst. (2007) 1–16.

[4] Y. Shahtaheri, C. Rausch, J. West, C. Haas, M. Nahangi, Managing risk in modular construction using dimensional and geometric tolerance strategies, Autom. Constr. 83 (2017) 303–315. https://doi.org/10.1016/j.autcon.2017.03.011.

[5] P.F. Court, C.L. Pasquire, G.F. Gibb, D. Bower, Modular Assembly with Postponement to Improve Health, Safety, and Productivity in Construction, Pract. Period. Struct. Des. Constr. 14 (2009) 81–89. https://doi.org/10.1061/(asce)1084-0680(2009)14:2(81).

[6] L. Jaillon, C.S. Poon, Y.H. Chiang, Quantifying the waste reduction potential of using prefabrication in building construction in Hong Kong, Waste Manag. 29 (2009) 309–320. https://doi.org/10.1016/j.wasman.2008.02.015.

[7] J.F. Zhang, J.J. Zhao, D.Y. Yang, E.F. Deng, H. Wang, S.Y. Pang, L.M. Cai, S.C. Gao, Mechanical-property tests on assembled-type light steel modular house, J. Constr. Steel Res. 168 (2020) 105981. https://doi.org/10.1016/j.jcsr.2020.105981.

[8] S.Y. Zhai, Y.F. Lyu, K. Cao, G.Q. Li, W.Y. Wang, C. Chen, Experimental study on bolted-cover plate corner connections for column-supported modular steel buildings, J. Constr. Steel Res. 189 (2022) 107060. https://doi.org/10.1016/j.jcsr.2021.107060.

[9] Y.F. Lyu, G.Q. Li, K. Cao, S.Y. Zhai, Y.B. Wang, L. Mao, M. ming Ran, Bending behavior of splice connection for corner-supported steel modular buildings, Eng. Struct. 250 (2022) 113460. https://doi.org/10.1016/j.engstruct.2021.113460.

[10] Y.F. Lyu, G.Q. Li, K. Cao, S.Y. Zhai, H. Li, C. Chen, Y.Z. Wang, Behavior of splice connection during transfer of vertical load in full-scale corner-supported modular building, Eng. Struct. 230 (2021) 111698. https://doi.org/10.1016/j.engstruct.2020.111698.

[11] P. Barnes, Off-site fabrication, BIM Princ. Pract. (2019) 109–112. https://doi.org/10.1680/bimpp.63693.109.

[12] K. Khan, Z. Chen, J. Liu, A. Khan, K. Javed, Axial compression behaviours of tubular sectioned C-shape continuous-supported steel walls in MSB, J. Constr. Steel Res. 188 (2022) 107009. https://doi.org/10.1016/j.jcsr.2021.107009.

[13] K. Khan, Z. Chen, J. Liu, A. Khan, Experimental and numerical study on planar multi-column walls behaviours with boundary supports, J. Constr. Steel Res. 186 (2021) 106880. https://doi.org/10.1016/j.jcsr.2021.106880.

[14] K. Khan, Z. Chen, J. Liu, A. Khan, Numerical and parametric analysis on compressive behaviours of continuous-supported wall systems in MSB, Structures. 33 (2021) 4053–4079. https://doi.org/10.1016/j.istruc.2021.07.001.

[15] R.M. Lawson, R.G. Ogden, R. Bergin, Application of Modular Construction in High-Rise Buildings, J. Archit. Eng. 18 (2012) 148–154. https://doi.org/10.1061/(asce)ae.1943-5568.0000057.

[16] A.W. Lacey, W. Chen, H. Hao, K. Bi, Review of bolted inter-module connections in modular

steel buildings, J. Build. Eng. 23 (2019) 207–219. https://doi.org/10.1016/j.jobe.2019.01.035.

[17] C.D. Annan, M.A. Youssef, M.H. El Naggar, Seismic overstrength in braced frames of modular steel buildings, J. Earthq. Eng. 13 (2009) 1–21. https://doi.org/10.1080/13632460802212576.

[18] Z. Chen, H. Li, A. Chen, Y. Yu, H. Wang, Research on pretensioned modular frame test and simulations, Eng. Struct. 151 (2017) 774–787. https://doi.org/10.1016/j.engstruct.2017.08.019.

[19] Y. Yu, Z. Chen, A. Chen, Experimental study of a pretensioned connection for modular buildings, Steel Compos. Struct. 31 (2019) 217–232. https://doi.org/10.12989/scs.2019.31.3.217.

[20] C. Kyung-Suk, K. Hyung-Joon, Analytical Models of Beam-Column joints in a Unit Modular Frame (in Korean), J. Comput. Struct. Eng. Inst. Korea. 27 (2014) 663–672. https://doi.org/10.7734/coseik.2014.27.6.663.

[21] M. Lawson, R. Ogden, C. Goodier, Design in Modular Construction, 2014. https://doi.org/10.1201/b16607.

[22] H.T. Thai, T. Ngo, B. Uy, A review on modular construction for high-rise buildings, Structures. 28 (2020) 1265–1290. https://doi.org/10.1016/j.istruc.2020.09.070.

[23] Z. Ye, K. Giriunas, H. Sezen, G. Wu, D.C. Feng, State-of-the-art review and investigation of structural stability in multi-story modular buildings, J. Build. Eng. 33 (2021) 101844. https://doi.org/10.1016/j.jobe.2020.101844.

[24] S. Srisangeerthanan, M.J. Hashemi, P. Rajeev, E. Gad, S. Fernando, Review of performance requirements for inter-module connections in multi-story modular buildings, J. Build. Eng. 28 (2020) 101087. https://doi.org/10.1016/j.jobe.2019.101087.

[25] A.W. Lacey, W. Chen, H. Hao, K. Bi, Structural response of modular buildings – An overview, J. Build. Eng. 16 (2018) 45–56. https://doi.org/10.1016/j.jobe.2017.12.008.

[26] C. Dan-Adrian, K.D. Tsavdaridis, A comprehensive review and classification of inter-module connections for hot-rolled steel modular building systems, J. Build. Eng. 50 (2022) 104006. https://doi.org/10.1016/j.jobe.2022.104006.

[27] E.F. Deng, L. Zong, Y. Ding, Z. Zhang, J.F. Zhang, F.W. Shi, L.M. Cai, S.C. Gao, Seismic performance of mid-to-high rise modular steel construction - A critical review, Thin-Walled Struct. 155 (2020) 106924. https://doi.org/10.1016/j.tws.2020.106924.

[28] Z. Chen, J. Liu, Y. Yu, Experimental study on interior connections in modular steel buildings, Eng. Struct. 147 (2017) 625–638. https://doi.org/10.1016/j.engstruct.2017.06.002.

[29] Z. Chen, J. Liu, Y. Yu, C. Zhou, R. Yan, Experimental study of an innovative modular steel building connection, J. Constr. Steel Res. 139 (2017) 69–82. https://doi.org/10.1016/j.jcsr.2017.09.008.

[30] K. Khan, Z. Chen, J. Liu, J. Yan, Simplified modelling of novel non-welded joints for modular steel buildings, Adv. Steel Constr. (2021).

[31] K. Khan, J.B. Yan, Finite Element Analysis on Seismic Behaviour of Novel Joint in Prefabricated Modular Steel Building, Int. J. Steel Struct. (2020). https://doi.org/10.1007/s13296-020-00320-w.

[32] K. Khan, J.-B. Yan, Numerical studies on seismic behaviour of a prefabricated multi storey modular steel building with new type bolted joints, Adv. Steel Constr. 17(1) (2021) 1–9. https://doi.org/10.18057/IJASC.2021.17.1.1.

[33] J. Peng, C. Hou, L. Shen, Progressive collapse analysis of corner-supported composite buildings, J. Build. Eng. 48 (2022).

[34] J. Peng, C. Hou, L. Shen, Numerical analysis of composite modular buildings under wind actions, J. Constr. Steel Res. 187 (2021).

[35] J. Peng, C. Hou, L. Shen, Lateral resistance of multi-story modular buildings using tenon-connected inter-module connections, J. Constr. Steel Res. 177 (2021).

[36] J. Peng, C. Hou, L. Shen, Numerical simulation of weld fracture using cohesive interface for novel inter-module connections, J. Constr. Steel Res. 174 (2020).

[37] B. Hajimohammadi, S. Das, H. Ghaednia, J. Dhanapal, Structural performance of registration

pin connection in VectorBloc modular construction system, J. Constr. Steel Res. 197 (2022) 107464. https://doi.org/10.1016/j.jcsr.2022.107464.

[38] J. Bowron, Locating pin assembly for a modular frame, WO2020010463A1, 2020.

[39] S.D. Pang, J.Y.R.L. Liew, Z. Dai, Y. Wang, Prefabricated Prefinished Volumetric Construction Joining Tech-niques Review, Modul. Offsite Constr. Summit Proc. (2016). https://doi.org/10.29173/mocs31.

[40] Z. Dai, T.Y.C. Cheong, S.D. Pang, J.Y.R. Liew, Experimental study of grouted sleeve connections under bending for steel modular buildings, Eng. Struct. 243 (2021) 112614. https://doi.org/10.1016/j.engstruct.2021.112614.

[41] Z. Dai, S.D. Pang, J.R. Liew, Axial load resistance of grouted sleeve connection for modular construction, Thin-Walled Struct. 154 (2020) 106883. https://doi.org/10.1016/j.tws.2020.106883.

[42] R. Ma, J. Xia, H. Chang, B. Xu, L. Zhang, Experimental and numerical investigation of mechanical properties on novel modular connections with superimposed beams, 232 (2021). https://doi.org/10.1016/j.engstruct.2021.111858.

[43] E.F. Deng, J.B. Yan, Y. Ding, L. Zong, Z.X. Li, X.M. Dai, Analytical and numerical studies on steel columns with novel connections in modular construction, Int. J. Steel Struct. 17 (2017) 1613–1626. https://doi.org/10.1007/s13296-017-1226-5.

[44] G. Zhang, L. Xu, Z. Li, Development and seismic retrofit of an innovative modular steel structure connection using symmetrical self-centering haunch braces, Eng. Struct. 229 (2021) 111671. https://doi.org/10.1016/j.engstruct.2020.111671.

[45] G. Nadeem, N.A. Safiee, N. Abu Bakar, I. Abd Karim, N.A. Mohd Nasir, Finite element analysis of proposed self-locking joint for modular steel structures, Appl. Sci. 11 (2021). https://doi.org/10.3390/app11199277.

[46] M. Liu, Y. Wang, S. Jia, Research on the mechanical properties of new plate-inner sleeve joint of steel modular frame (in Chinese), Steel Constr. (2018).

[47] F. Shi, Y. Li, Innovative inner sleeve composite bolted connections for modular steel constructions: Experimental and numerical studies, J. Build. Eng. (2022) 105624. https://doi.org/10.1016/j.jobe.2022.105624.

[48] R.J. Liew, Z. Dai, Y.S. Chau, Steel Concrete Composite Systems for Modular Construction of High-rise Buildings, (2018). https://doi.org/10.4995/asccs2018.2018.7220.

[49] J.Y.R. Liew, Y.S. Chua, Z. Dai, Steel concrete composite systems for modular construction of high-rise buildings, Structures. 21 (2019) 135–149. https://doi.org/10.1016/j.istruc.2019.02.010.

[50] R. Sanches, O. Mercan, B. Roberts, Experimental investigations of vertical post-tensioned connection for modular steel structures, Eng. Struct. 175 (2018) 776–789. https://doi.org/10.1016/j.engstruct.2018.08.049.

[51] R. Sanches, O. Mercan, Vertical post-tensioned connection for modular steel buildings, (2019) 1–8.

[52] A.W. Lacey, W. Chen, H. Hao, K. Bi, New interlocking inter-module connection for modular steel buildings: Experimental and numerical studies, Eng. Struct. 198 (2019). https://doi.org/10.1016/j.engstruct.2019.109465.

[53] A.W. Lacey, W. Chen, H. Hao, K. Bi, F.J. Tallowin, Shear behaviour of post-tensioned inter-module connection for modular steel buildings, J. Constr. Steel Res. 162 (2019) 105707. https://doi.org/10.1016/j.jcsr.2019.105707.

[54] K. Tayyebi, M. Sun, Design of direct-formed square and rectangular hollow section stub columns, J. Constr. Steel Res. 178 (2021) 106499. https://doi.org/10.1016/j.jcsr.2020.106499.

[55] Monash University-modular construction codes board, Handbook for the Design of modular structures, Monash University, 2017.

[56] M. Theofanous, Studies of the Nonlinear Response of Stainless Steel Structures, Imperial College London, 2010.

[57] M. Theofanous, L. Gardner, Testing and numerical modelling of lean duplex stainless steel

hollow section columns, Eng. Struct. 31 (2009) 3047–3058. https://doi.org/10.1016/j.engstruct.2009.08.004.

[58] J. Hou, X. Wang, J. Liu, Z. Chen, X. Zhong, Study on the stability bearing capacity of multi-column wall in modular steel building, Eng. Struct. 214 (2020) 110648. https://doi.org/10.1016/j.engstruct.2020.110648.

[59] ABAQUS (2013), User manual Version 6.13., DS SIMULIA Corp, Provid. RI, USA. (2013) 1–847.

[60] B.K.J.R. Rasmussen, G.J. Hancock, Stainless Steel Structural Members . Outline of Test Program, 119 (2006) 2349–2367.

[61] R.B. Cruise, L. Gardner, Residual stress analysis of structural stainless steel sections, J. Constr. Steel Res. 64 (2008) 352–366. https://doi.org/10.1016/j.jcsr.2007.08.001.

[62] I. Arrayago, K.J.R. Rasmussen, Influence of the imperfection direction on the ultimate response of steel frames in advanced analysis, J. Constr. Steel Res. 190 (2022) 107137. https://doi.org/10.1016/j.jcsr.2022.107137.

[63] X. Wang, J. Hou, J. Liu, Z. Tian, Study of effective length factor for column in steel multi-column wall (in Chinese), in: 18th Natl. Symp. Mod. Struct. Eng., 2018: pp. 36–40.

[64] J. Hou, Stability of Multi-column Wall in Modular Steel Structures (MS thesis in Chinese), Tianjin University, 2018.

[65] Martijn Visser, What is a stress singularity in SOLIDWORKS Simulation?, Elit. Appl. Eng. CAD2M. (2018). https://blogs.solidworks.com/tech/2018/07/what-is-a-stress-singularity-in-solidworks-simulation.html.

[66] LESLIE LANGNAU, Avoiding singularities in FEA boundary conditions, World (A Des. World Resour. (2021). https://www.3dcadworld.com/avoiding-singularities-in-fea-boundary-conditions/.

[67] Łukasz Skotny, Stress singularity – an honest discussion, Enterfea. (2017). https://enterfea.com/stress-singularity-an-honest-discussion/.

[68] H.J. Fogg, L. Sun, J.E. Makem, C.G. Armstrong, T.T. Robinson, Singularities in structured meshes and cross-fields, CAD Comput. Aided Des. 105 (2018) 11–25. https://doi.org/10.1016/j.cad.2018.06.002.

[69] Y. Pandya, A. Parey, Failure path based modified gear mesh stiffness for spur gear pair with tooth root crack, Eng. Fail. Anal. 27 (2013) 286–296. https://doi.org/10.1016/j.engfailanal.2012.08.015.

[70] M. Acin, Stress singularities, stress concentrations and mesh convergence, Acin.Net (Engineering My Life). (2015). http://www.acin.net/2015/06/02/stress-singularities-stress-concentrations-and-mesh-convergence/.

[71] G. İrsel, The effect of using shell and solid models in structural stress analysis, Vibroengineering Procedia. 27 (2019) 115–120. https://doi.org/10.21595/vp.2019.20977.

[72] Y. Liu, G. Glass, Effects of mesh density on finite element analysis, SAE Tech. Pap. 2 (2013). https://doi.org/10.4271/2013-01-1375.

[73] J. Ye, S.M. Mojtabaei, I. Hajirasouliha, Local-flexural interactive buckling of standard and optimised cold-formed steel columns, J. Constr. Steel Res. 144 (2018) 106–118. https://doi.org/10.1016/j.jcsr.2018.01.012.

[74] D.S. Castanheira, L.R.O. De Lima, P.C.G. Da Silva Vellasco, A.T. Da Silva, M.C. Rodrigues, Numerical modelling of rectangular cold-formed steel and composite columns, Proc. Inst. Civ. Eng. Struct. Build. 172 (2019) 805–818. https://doi.org/10.1680/jstbu.18.00057.

[75] B. Xu, J. Xia, R. Ma, J. Wang, X. Chen, H. Chang, L. Zhang, Investigation on true stress-strain curves of flat and corner regions of cold-formed section using 3D digital image correlation method, Adv. Civ. Eng. 2019 (2019). https://doi.org/10.1155/2019/3138176.

[76] E. 1993-1-5, Eurocode 3 - Design of steel structures - Part 1-5: Plated structural elements, 2006.

[77] J.B. Yan, J. Feng, Y.B. Luo, Y. Du, Compression behaviour of stainless-steel stub square tubular columns at cold-region low temperatures, J. Constr. Steel Res. 187 (2021).

https://doi.org/10.1016/j.jcsr.2021.106984.

[78] Y. Du, M. Fu, Z. Chen, J.B. Yan, Z. Zheng, Axial compressive behavior of CFRP confined rectangular CFT columns using high-strength materials: Numerical analysis and carrying capacity model, Structures. 36 (2022) 997–1020. https://doi.org/10.1016/j.istruc.2021.12.061.

[79] GB50017-2017, Standard for design of steel structures (in Chinese), (2017).

[80] Y. Chen, C. Hou, J. Peng, Stability study on tenon-connected SHS and CFST columns in modular construction, Steel Compos. Struct. 30 (2019) 185–199. https://doi.org/10.12989/scs.2019.30.2.185.

[81] A.W. Lacey, W. Chen, H. Hao, Experimental methods for inter-module joints in modular building structures – A state-of-the-art review, J. Build. Eng. 46 (2022) 103792. https://doi.org/10.1016/j.jobe.2021.103792.

[82] R. Sanches, O. Mercan, B. Roberts, Experimental investigations of vertical post-tensioned connection for modular steel structures, Eng. Struct. 175 (2018) 776–789. https://doi.org/10.1016/j.engstruct.2018.08.049.

[83] ASTMP, Grade Q345 Imported Tube does not conform to grade S355 | Association of Steel Tube and Pipe Manufacturers, (n.d.). https://www.astpm.com/grade-q345-imported-tube-does-not-conform-to-grade-s355/ (accessed April 24, 2021).

[84] K. Rzeszut, Post-Buckling Behaviour of Steel Structures with Different Types of Imperfections, Appl. Sci. 12 (2022). https://doi.org/10.3390/app12189018.

[85] J. Yan, B. Zhang, X. Yu, J. Xie, Thin-Walled Structures Mechanical properties of stainless steel QN1906Mo at sub-zero temperatures : Tests and stress – strain models, Thin-Walled Struct. 179 (2022) 109727. https://doi.org/10.1016/j.tws.2022.109727.

[86] J.B. Yan, Y.L. Luo, C. Liang, X. Lin, Y.B. Luo, L. Zhang, Compression behaviours of concrete-filled Q690 high-strength steel tubular columns at low temperatures, J. Constr. Steel Res. 187 (2021) 106983. https://doi.org/10.1016/j.jcsr.2021.106983.

[87] J.B. Yan, X. Yang, Y. Luo, P. Xie, Y.B. Luo, Axial compression behaviours of ultra-high performance concrete-filled Q690 high-strength steel tubes at low temperatures, Thin-Walled Struct. 169 (2021) 108419. https://doi.org/10.1016/j.tws.2021.108419.

[88] J.B. Yan, T. Wang, X. Dong, Compressive behaviours of circular concrete-filled steel tubes exposed to low-temperature environment, Constr. Build. Mater. 245 (2020) 118460. https://doi.org/10.1016/j.conbuildmat.2020.118460.

[89] J.B. Yan, W.J. Xie, Y. Luo, T. Wang, Behaviours of concrete stub columns confined by steel tubes at cold-region low temperatures, J. Constr. Steel Res. 170 (2020) 106124. https://doi.org/10.1016/j.jcsr.2020.106124.

[90] J.B. Yan, X. Dong, T. Wang, Axial compressive behaviours of square CFST stub columns at low temperatures, J. Constr. Steel Res. 164 (2020) 105812. https://doi.org/10.1016/j.jcsr.2019.105812.

[91] J.B. Yan, Y.L. Luo, L. Su, X. Lin, Y.B. Luo, L. Zhang, Low-temperature compression behaviour of square CFST columns using Q960 ultra-high strength steel, J. Constr. Steel Res. 183 (2021). https://doi.org/10.1016/j.jcsr.2021.106727.

[92] M.X. Xiong, J.B. Yan, Buckling length determination of concrete filled steel tubular column under axial compression in standard fire test, Mater. Struct. Constr. 49 (2016) 1201–1212. https://doi.org/10.1617/s11527-015-0570-1.

[93] H. Chen, C. Ke, C. Chen, G. Li, Study on the shear behavior of inter-module connection with a bolt and shear key fi tting for modular steel buildings, 0 (2022) 1–16. https://doi.org/10.1177/13694332221122547.

[94] J. Wang, B. Uy, D. Li, Analysis of demountable steel and composite frames with semi-rigid bolted joints, Steel Compos. Struct. 28 (2018) 363–380. https://doi.org/10.12989/scs.2018.28.3.363.

[95] Z. Xu, T. Zayed, Y. Niu, Comparative analysis of modular construction practices in mainland China, Hong Kong and Singapore, J. Clean. Prod. 245 (2020). https://doi.org/10.1016/j.jclepro.2019.118861.

[96] A. Shapoval, V. Courtillot, Influence of the P-delta Effect and Stiffness Irregularity on the Structural Behavior of Reinforced Concrete Buildings Influence of the P-delta Effect and Stiffness Irregularity on the Structural Behavior of Reinforced Concrete Buildings, in: J. Phys. Conf. Ser., IOP, 2022. https://doi.org/10.1088/1742-6596/2287/1/012047.

[97] J.B. Yan, X. Dong, J.S. Zhu, Behaviours of stub steel tubular columns subjected to axial compression at low temperatures, Constr. Build. Mater. 228 (2019). https://doi.org/10.1016/j.conbuildmat.2019.116788.

[98] T.G. Singh, T. Chan, Effect of access openings on the buckling performance of square hollow section module stub columns, J. Constr. Steel Res. 177 (2021) 106438. https://doi.org/10.1016/j.jcsr.2020.106438.

[99] EN 1993-1-1, Eurocode 3: Design of steel structures - Part 1-1: General rules and rules for buildings, 2005.

[100] L. Srikanth, Design of steel structures based on BS5950, 2020. https://doi.org/10.13140/RG.2.2.25897.75364.

[101] UK steel construction information, Member design - SteelConstruction.info, (n.d.). https://www.steelconstruction.info/Member_design#cite_note-NAtoBSEN1993-1-1-2 (accessed June 11, 2021).

[102] NA to CYS EN 1993-1-1:2005, Eurocode 3: Design of steel structures Part 1-1: General rules and rules for buildings, 2005 (2014).

[103] B. Charbrolin, Technical steel research-Partial safety factors for resistance of steel elements to EC3 and EC4 — Calibration for various steel products and failure criteria, 2002.

[104] Publications Office of the EU, Partial safety factors for resistance of steel elements to EC3 and EC4 - Calibration for various steel products and failure criteria, (n.d.). https://op.europa.eu/en/publication-detail/-/publication/1602ab5d-3994-4464-8c44-664016689b1e (accessed June 19, 2021).

[105] CSA-S16-09, CSA standard-Design of steel structures, 2009.

[106] ANSI/AISC 360-16, AISC360/16 Specification for Structural Steel Buildings-An American National Standard, 2016.

[107] S. Pinarbasi, T. Genc, E. Akpinar, F. Okay, Comparison of Design Guidelines for Hot-Rolled I-Shaped Steel Compression Members according to AISC 360-16 and EC3, Adv. Civ. Eng. 2020 (2020). https://doi.org/10.1155/2020/6853176.

Nomenclature

IMC, inter-modular connections; MSS, modular steel structure; TSS, traditional steel structures; SHS, steel-hollow sections; HSS, high strength steel; a_c, elliptical tube's longest diameter; b_c, elliptical tube's shortest diameter; D, tube's length; B, tube's width; r, cross-section root radii; L_c, tube's height; L_c/r, member slenderness ratio; t_c, tube's thickness; d, shear-key length; b, shear-key width; t_t, shear-key thickness; L_t, shear-key height; D/t_c, cross-sectional slenderness ratio; FEM/FEA, finite element model/analysis; E_s, tube elastic modulus; f_y, tube yield strength; f_u, tube ultimate strength; $E_{s,w}$, tubes' flat wall elastic modulus; $f_{y,w}$, tubes' flat wall yield strength; $f_{u,w}$, tubes' flat wall ultimate strength; $E_{s,c}$, stainless tubes' corner elastic modulus; $f_{y,c}$, stainless tubes' corner yield strength; $f_{u,c}$, stainless tubes' corner ultimate strength; P_u, ultimate compressive resistance; P_y, yield resistance; P_{cr}, critical load; $P_{u,c}$, ultimate cross-sectional resistance via EC3:1-1, represented as EC3-C; $P_{u,b}$, ultimate members buckling resistance via EC3:1-1, described as EC3-B; $P_{u,Test}$, ultimate resistance via test; $P_{u, FE}$, ultimate resistance via FEA; $P_{u, EC3}$, ultimate compressive resistance via EC3:1-1; $P_{u, AISC}$, ultimate compressive resistance via AISC360-16; $P_{u, CSA}$, ultimate compressive resistance via CSA S16; $P_{u, GB}$, ultimate compressive resistance via GB50017; K_e, initial stiffness; Δ_u, axial shortening; DI, ductility index; $P_{45\%}$, 45% load of P_u; $\Delta_{45\%}$, axial shortening at $P_{45\%}$; $\Delta_{85\%}$, axial shortening at $P_{85\%}$; Cov, coefficient of variation; e, eccentricity; GB, global buckling; IB, inward buckling; OB, outward buckling; σ_T/σ_E= True/Engineering stress; $\varepsilon_T/\varepsilon_E$ = True/Engineering strain; γ_M , partial safety factor in EC3:1-1; $\alpha_1, \alpha_2,$ and α_3, partial safety factors in GB50017